A&A, 711, A240 (2026)
https://doi.org/10.1051/0004-6361/202557830


Astronomy & Astrophysics

# JOYS+: Analyses of $OCN^-$, $N_2O$, NO, and complex cyanides in ices

## Thermal processing results in a modest increase of $OCN^-$ ice

P. Nazari[1,⋆], N. Brunken[2], Y. Chen[2], K. Slavicinska[2], E. F. van Dishoeck[2,3], W. R. M. Rocha[2], A. C. A. Boogert[4], M. G. Navarro[5], V. J. M. Le Gouellec[6,7], L. Francis[2], Ł. Tychoniec[2], A. Caratti o Garatti[8], C. Gieser[9], T. P. Greene[10], and P. J. Kavanagh[11]

[1] European Southern Observatory, Karl-Schwarzschild-Strasse 2, 85748 Garching, Germany
[2] Leiden Observatory, Leiden University, PO Box 9513, 2300 RA Leiden, The Netherlands
[3] Max Planck Institut für Extraterrestrische Physik (MPE), Giessenbachstrasse 1, 85748 Garching, Germany
[4] Institute for Astronomy, University of Hawai'i at Manoa, 2680 Woodlawn Drive, Honolulu, HI 96822, USA
[5] INAF–Osservatorio Astronomico di Roma, Via di Frascati 33, 00078 Monte Porzio Catone, Italy
[6] Institut de Cienciès de l'Espai (ICE-CSIC), Campus UAB, Carrer de Can Magrans S/N, 08193 Cerdanyola del Vallès, Spain
[7] Institut d'Estudis Espacials de Catalunya (IEEC), c/ Gran Capitá 2–4, 08034 Barcelona, Spain
[8] INAF–Osservatorio Astronomico di Capodimonte, Salita Moiariello 16, 80131 Napoli, Italy
[9] Max Planck Institute for Astronomy, Königstuhl 17, 69117 Heidelberg, Germany
[10] IPAC, California Institute of Technology, MC 100-22, 1200 E. California Blvd., Pasadena, CA 91125, USA
[11] Department of Physics, Maynooth University, Maynooth, Co. 13 Kildare, Ireland

Received 25 October 2025 / Accepted 22 April 2026

**ABSTRACT**

*Context.* Nitrogen-bearing molecules are generally more difficult to observe than oxygen-bearing ones in both gas and ice, mainly due to the lower abundance of nitrogen in the interstellar medium. Therefore, the formation pathways of many of these species is still under debate.
*Aims.* Studies prior to the launch of the *James Webb* Space Telescope (JWST) did not have the sensitivity to observe ices toward the youngest and most deeply embedded Class 0 objects. The time is now ripe to study nitrogen-bearing molecules toward ice-rich Class 0 and Class I objects with the JWST. Here we focus on $OCN^-$, $CH_3CN$, $C_2H_5CN$, NO, and $N_2O$ in ices to better understand their formation.
*Methods.* We used the data from JWST Observations of Young protoStars (JOYS+) program. Particularly, we studied the objects that have the JWST NIRSpec-IFU observations (8 Class 0 and 11 Class I) to measure the ice column densities of the targeted molecules.
*Results.* We firmly detect $OCN^-$ in ices for all these objects, tentatively detect $CH_3CN$, $C_2H_5CN$, and $N_2O$ toward three sources, and find upper limits on the NO abundance in ices. The $OCN^-/CO_2$ ratios are found to be higher by a factor of ∼2–3 for the objects that have a visible $CO_2$ (15.2 μm) double peak (a sign of ice thermal processing), which points to the moderate effect of temperature on $OCN^-$ production. Considering $H_2O$, $CO_2$, and $OCN^-$ relations with $A_V$, we tentatively find that $OCN^-$ forms at a later stage compared to $H_2O$ and $CO_2$. We find that the ratios of $CH_3CN$, $C_2H_5CN$, and $N_2O$ with respect to $OCN^-$ are relatively constant within one order of magnitude across our objects, likely suggesting that they have similar ice environments. The upper limit abundances of NO are around one order of magnitude lower than what was previously predicted in ices of a mature protoplanetary disk to explain the gas-phase detection of this molecule in the disk. This indicates that gas-phase NO may be a product of another molecule such as $N_2O$ in the ices.
*Conclusions.* We conclude that after $OCN^-$ forms, it can increase at higher temperatures by only a factor of ∼2–3, and thus $OCN^-$ detection alone does not imply ice heating. Large-sample studies of $OCN^-$ toward pre-stellar cores will be useful to further confirm the formation timeline of this molecule.

**Key words.** astrochemistry – solid state: volatile – stars: protostars – ISM: abundances – ISM: molecules

## 1. Introduction

Compared to oxygen, nitrogen is a factor of ∼5 less abundant in the interstellar medium (ISM; Wilson & Rood 1994), and therefore, molecules containing nitrogen are also relatively less abundant and generally more difficult to observe in ice and gas. However, understanding the formation of nitrogen-bearing species is crucial, considering their contribution to the formation of the amino acids and nucleobases necessary for the formation of habitable worlds. In ices, $OCN^-$ is one of the nitrogen-bearing molecules along with $NH_3$ and $NH_4^+$ that often shows a clear and strong absorption feature (e.g., Schutte & Khanna 2003; van Broekhuizen et al. 2004; Bottinelli et al. 2010; Boogert et al. 2008, 2015). Telescopes, especially those from the ground, such as ESO's Very Large Telescope (VLT) and NASA's InfraRed Telescope Facility (IRTF), have observed $OCN^-$ toward low- and high-mass protostellar systems (van Broekhuizen et al. 2005; Boogert et al. 2022). However, for low-mass objects, those observations were biased toward the brighter, less embedded,

⋆ Corresponding author: pooneh.nazari@eso.org

and more evolved objects (i.e., Class I sources) rather than the younger and more embedded ice-rich ones (i.e., Class 0 sources). With the launch of the *James Webb* Space Telescope (JWST; Gardner et al. 2023), we have a unique opportunity to also search for $OCN^-$ and other molecules in the ices of the fainter Class 0 objects (Yang et al. 2022) and dense pre-stellar cores (McClure et al. 2023).

One of the clearest and least blended features of $OCN^-$ at around 4.6 μm falls in the range observed by the Near-Infrared Spectrograph (NIRSpec; Jakobsen et al. 2022) mounted on the JWST. Previous laboratory and observational studies have suggested that $OCN^-$ forms in a CO-rich environment and survives in a warmer polar environment (van Broekhuizen et al. 2005; Öberg et al. 2011; Boogert et al. 2022). However, observationally we lacked data points for Class 0 objects before the launch of JWST. Thus, only now can the formation and evolution of $OCN^-$ be investigated further through JWST observations. To date, a few JWST studies have analyzed the 4.6 μm feature of $OCN^-$ in protostellar ices; however, those studies together account for only five low- and high-mass protostellar systems (Nazari et al. 2024; Tyagi et al. 2025). Here our aim is to increase the sample size for low-mass objects and to study the formation of $OCN^-$.

The only carbon-bearing molecule with at least six atoms, i.e., a complex organic molecule (COM), that was firmly detected in ices before the launch of JWST was methanol ($CH_3OH$; Gibb et al. 2000, 2004). This was simply due to the lack of sensitivity and spectral resolution of previous telescopes to observe species with such low abundances ($\lesssim 10^{-7}$) and low band strengths (a few $10^{-18}$ cm molecule$^{-1}$) even though hints of COMs had been observed (Schutte et al. 1999; Öberg et al. 2011; Terwisscha van Scheltinga et al. 2021). Over the past two years JWST has detected several oxygen-bearing COMs for the first time in ices (Rocha et al. 2024; Chen et al. 2024; Rayalacheruvu et al. 2025). Due to the lower abundance of nitrogen in comparison with oxygen, nitrogen-bearing COMs are even more difficult to observe. Among those, the most abundant one in the gas phase is methyl cyanide ($CH_3CN$), and after that a few molecules show similar abundances, including ethyl cyanide ($C_2H_5CN$; e.g., Calcutt et al. 2018; Yang et al. 2021; Nazari et al. 2021, 2022; Chahine et al. 2022). Therefore, these may be two of the best candidates when searching for them in ices. In the wavelength range that JWST observes (~1–28 μm), these two molecules have their strongest transitions at around 4.5 μm (Moore et al. 2010; Rachid et al. 2022). After this, the best transitions are in the ~7–8 μm regime of the JWST Mid-Infrared Instrument (MIRI; Wright et al. 2023). Both $CH_3CN$ and $C_2H_5CN$ have been tentatively detected in protostellar ices of the Investigating Protostellar Accretion (IPA) program by analysis of the 4.5 μm feature (Nazari et al. 2024). For this work, our aim was to expand on that work by increasing the sample size and additionally considering the transitions in the ~7–8 μm wavelength range. This will also improve our understanding of complex cyanide formation, especially considering the long-lasting debate on this topic (Huntress & Mitchell 1979; Herbst 1980; Walsh et al. 2014; Garrod et al. 2022; Nazari et al. 2023).

Nitrogen is expected to have a refractory and a volatile reservoir. The amount of nitrogen in each component is uncertain; the dusty refractory component is found to be dominant in comet 67P (Fray et al. 2016; Bardyn et al. 2017; Rubin et al. 2019). By updating the band strength of $NH_4^+$, Slavicinska et al. (2025) found that a major component of nitrogen (with abundances of up to ~20% with respect to water) could be stored in the semi-refractory salts in protostellar systems. Here, we consider putting limits on the volatile $N_2O$ and NO ice abundances and investigate whether these molecules could be important nitrogen sinks. $N_2O$ ice has been tentatively detected toward other protostellar systems (Nazari et al. 2024; Rocha et al. 2025), with an ice abundance of just below unity with respect to $OCN^-$ toward Ced 110 IRS4A. Moreover, NO has been recently detected in the gas of protoplanetary disk Oph-IRS 48 (Brunken et al. 2022) and the models of Leemker et al. (2023) predict that NO and/or $N_2O$ may be present in ices.

For this paper we studied $OCN^-$, $CH_3CN$, $C_2H_5CN$, NO, and $N_2O$ in ices of the objects covered by the JWST Observations of Young protoStars (JOYS+) program (van Dishoeck et al. 2025). The sample covers ~30 low- and high-mass protostellar objects (Beuther et al. 2023; Gieser et al. 2023; Francis et al. 2024; van Gelder et al. 2024b). The low-mass protostars of the sample include both Class 0 and Class I objects. The protostellar systems observed to date by JWST within the JOYS+ program or otherwise show a diversity in their outflow and jet structures (Ray et al. 2023; Caratti o Garatti et al. 2024; Narang et al. 2024; Tychoniec et al. 2024), in addition to their ice and gas-phase spectral features (e.g., Federman et al. 2024; Neufeld et al. 2024; van Gelder et al. 2024b; Salyk et al. 2024). In the JOYS sample for example, van Gelder et al. (2024a) found that although two of the sources (B1-c and L1448-mm) were particularly line-rich (in either emission or absorption), many of them only showed detection of gaseous $H_2O$ and $CO_2$ lines. Moreover, Brunken et al. (2024b) investigated the ice abundances of CO, $CO_2$, and their isotopologs in the JOYS+ sample and found that the $^{12}CO_2/^{13}CO_2$ ratios in ices range between ~ 70−120 and that the $^{12}CO/^{13}CO$ values are relatively elevated. In terms of COMs, B1-c and IRAS 2A in particular have clearly shown the signature COM absorption features with MIRI (Rocha et al. 2024; Chen et al. 2024). For this paper, we focused on a subset of the low-mass sample that has NIRSpec observations (a total of 19 sources).

We first give an overview of the data and the sources in Sect. 2. Next, in Sect. 3 we explain our methods of spline fitting and continuum determination. In Sect. 4 we describe the spectral fitting and column density measurement. The results for the ratios of $CH_3CN$, $C_2H_5CN$, and $N_2O$ with respect to $OCN^-$ are presented in Sect. 4.5. In Sect. 5 we discuss the $OCN^-/CO$ and $OCN^-/CO_2$ ratios and their significance to $OCN^-$ formation. We conclude in Sect. 6.

## 2. Observations

In this work we use the NIRSpec-IFU (Böker et al. 2022) and MIRI-MRS (Argyriou et al. 2023) data of the JOYS+ program (PIDs: 1186, 1236, 1290, 1960; PIs: T.P. Greene, M.E. Ressler, and E.F. van Dishoeck). Although the entire JOYS+ sample covers more protostellar systems, only 16 of them have NIRSpec data. As this work primarily uses the NIRSpec data, we focus on these 16 systems. Four are binaries, thus resulting in 20 separate Class 0/I objects. From this sample, we removed L1448-IRS1 as it shows a high level of noise, and thus any conclusions on the targeted molecules in its ices are not particularly meaningful. As a result, 19 objects were analyzed. The data description and reduction are explained in detail in van Gelder et al. (2024a, MIRI-MRS), Brunken et al. (2024b), and Le Gouellec et al. (2025, NIRSpec), and hence we only briefly summarize the observations and analysis here.

The NIRSpec data were taken using either the PRISM or G235H grating at the shorter wavelengths and the G395M or G395H grating at the longer wavelengths. A four-point dither

with the NRSIRS2RAPID readout pattern was used. The data were reduced using additional corrections to the standard JWST pipeline to increase the data quality. More information on the specifics can be found in Brunken et al. (2024b) and Le Gouellec et al. (2025). The MIRI-MRS data were mostly taken using a two-point dither pattern except for B1-c, which was observed using a four-point dither pattern. The data were obtained using the FASTR1 mode. All observations include the four MIRI channels with short, medium, and long gratings fully covering the 4.9–28.6 μm range. The data reduction procedure is explained in van Gelder et al. (2024a).

For this work we used an on-source location (i.e., the peak continuum position at 5.251 μm) to extract the spectra. This approach is similar to that used in other JOYS+ papers (Rocha et al. 2024; Chen et al. 2024; Brunken et al. 2024b). Therefore, the column density ratios of the species considered here and those studied in other JOYS+ papers can be determined referring to the same regions around our objects. The on-source spectral extraction positions in the NIRSpec cubes are given in Table A.1. There was a slight mismatch between the continuum right ascension (RA) and declination (Dec.) at the same wavelength between NIRSpec and MIRI cubes due to astrometry errors of the instruments. This error varies between objects and can be close to zero for some objects, but for some others it can be as large as ∼0.5″. Thus, for the MIRI spectra we extracted the spectra from the 5.251 μm continuum peak position found in the MIRI cubes rather than using the same RA and Dec. found from NIRSpec continuum peak positions. The spectra were extracted in a similar way to Brunken et al. (2024b) using a cone aperture with diameter of three times $1.22\lambda/D$ radians, where $D$ is the telescope mirror diameter of 6.5 m. This method ensures the inclusion of a maximum amount of flux without overlap between objects within binaries, although this will be unavoidable at longer MIRI wavelengths. The root mean square (rms) error on the extracted NIRSpec spectra are calculated using the error plane of the data cubes and considering two relatively featureless regions. In this procedure the error is first turned into optical depth ($\tau$) scale from flux ($f$) scale using

$$\mathrm{err}_{\tau,\lambda} = \mathrm{err}_{\mathrm{f},\lambda}/\mathrm{f}_{\lambda}. \quad (1)$$

The rms of $\mathrm{err}_{\tau,\lambda}$ about its mean is reported as the optical depth rms error in Table A.1.

## 3. Band identification, spline, and continuum fitting

In this paper, we mainly focus on the ∼4.4–4.7 μm region where $OCN^-$ and complex cyanides are expected to have their strongest absorption bands. Unfortunately, CO rotational–vibrational transitions (v=1–0) are also located in this spectral region (Federman et al. 2024; Rubinstein et al. 2024). They are often detected toward our objects and can affect the ice bands. The other portion of the spectrum (around 5.35 μm) used in this work for NO (see Sect. 4.4) also shows gas-phase lines (e.g., from CO and $H_2O$).

Therefore, we first fitted a baseline (magenta curve in Fig. 1) to the bottom of the emission lines or the top of the absorption lines. This baseline was then used for the ice fitting, although we overlaid our final ice model on the full spectrum with gas-phase lines for a consistency check (Sect. 4). For this spline fitting, we followed a similar method to Rubinstein et al. (2024) and used the `pybaselines` package in Python (Erb 2024). We used their penalized spline asymmetric least squares algorithm via the `pspline_asls` function. We altered three main parameters of this function per source to obtain a well-fitted spline to the bottom of the emission lines or the top of the absorption lines. These three parameters were `lam`, the smoothing parameter; `num_knots`, the number of knots for the spline; and `p`, the penalizing weighting factor that indicates whether to fit the bottom of the gas-phase emission lines or the top of the gas-phase absorption lines. The final fitted baselines to the spectra in the ∼4.4–4.8 μm are shown in Fig. 1 for B1-c (i.e., one of the least extreme objects in showing CO gas-phase lines) and L1448-mm (i.e., one of the most extreme cases in showing bright CO emission lines), while those for the rest of the objects are presented in Fig. B.1.

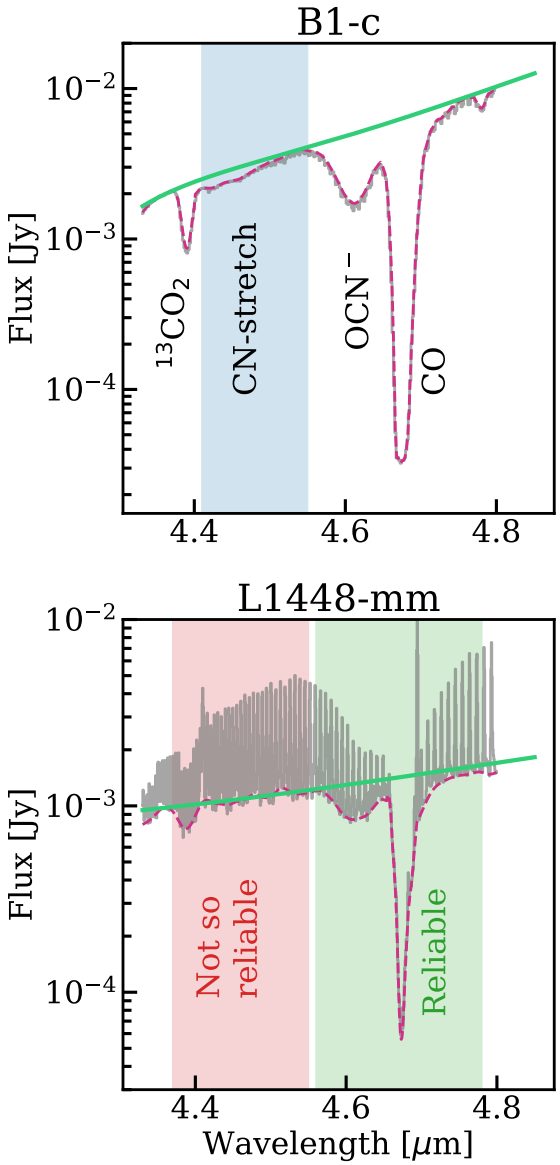


**Fig. 1.** Example of spline fitting for two of our objects. The data are in gray, and the dashed magenta line shows the fitted spline to the bottom of the gas-phase emission or the top of the gas-phase absorption lines. Most of our objects were too line rich for a reliable measurement of column densities of the weak features at 4.45 μm (shaded red area), but the spline fitting was reliable for the stronger features such as $OCN^-$ and CO (shaded green area) even for these sources. An extreme case in gas-phase emission lines is L1448-mm, which is presented in the bottom panel. Both weaker and stronger features of B1-c (top panel) after spline fitting, despite the presence of some gas-phase lines, are reliable for further analysis. The green solid line shows the fitted local continuum.

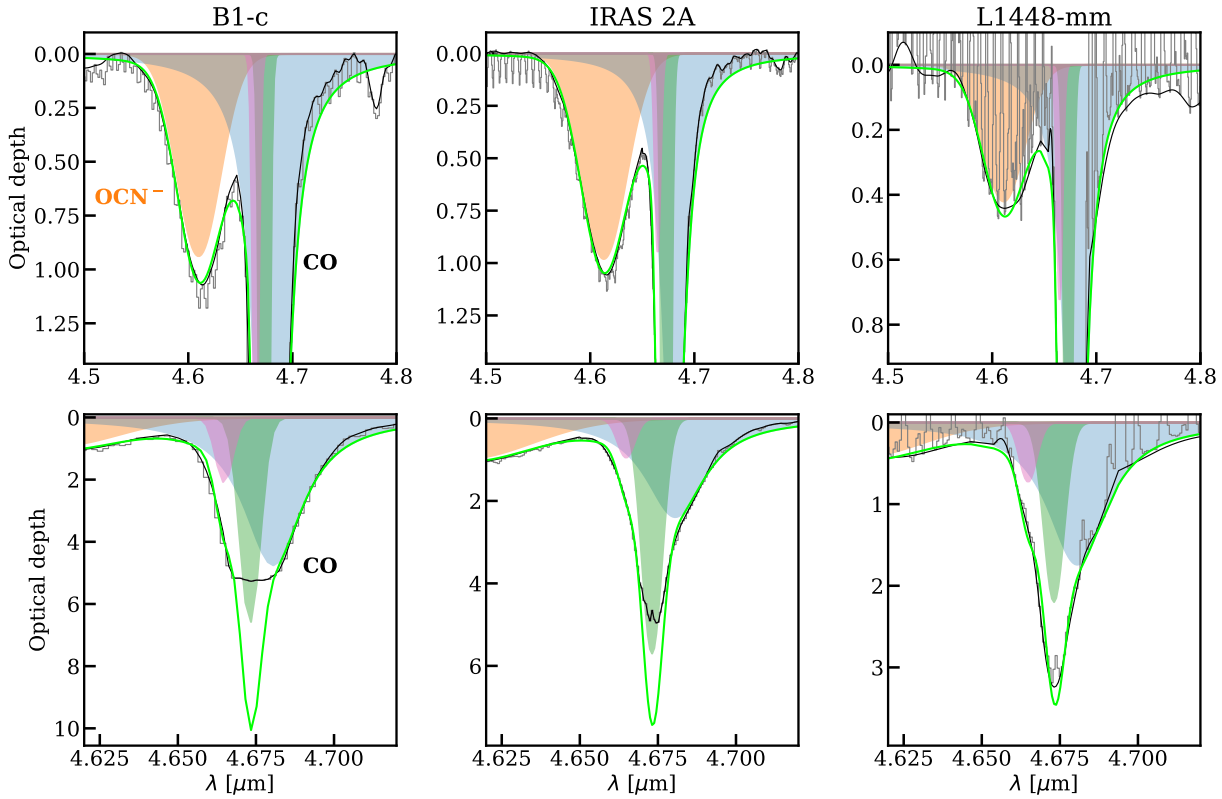


**Fig. 2.** Our fits to the $OCN^-$ and CO absorption features toward three of the studied objects. As explained in the text, $OCN^-$ is fitted simultaneously with CO ice. The orange shaded area shows the fit to the $OCN^-$ feature. The shaded blue, green, and pink areas show the Lorentzian and Gaussian components fitted to the CO feature. The total fit is presented as a solid lime green line. The solid black line shows the spline that is fitted to the bottom of the gas-phase emission or the top of the gas-phase absorption lines where the data are overplotted in gray. We note that the top and bottom rows have different scales; the top row highlights the $OCN^-$ fits and the bottom row shows the CO fits. For some objects, such as B1-c and IRAS 2A where the CO feature becomes saturated close to the noise level, the bottom of the CO feature is ignored when fitting the data and only the wings of the CO band, which are well above the noise level, are fitted. The fits for the other objects considered in this work are given in Figs. B.2 and B.3.

Next, we fitted a local continuum (green curve in Fig. 1, $F_\lambda^{\rm cont}$) to this region using the polynomial function method of the ENIIGMA fitting tool (Rocha et al. 2021). This method is commonly used when analyzing ice bands (e.g., Boogert et al. 2022; Nazari et al. 2024; Slavicinska et al. 2024). The flux ($F_\lambda^{\rm data}$) was then converted to optical depth ($\tau_\lambda$) via $-\ln(F_\lambda^{\rm data}/F_\lambda^{\rm cont})$. The fitted continuum in the region between 4.4 and 4.8 μm for B1-c and L1448-mm are presented in Fig. 1, while those for the rest of our objects are shown in Fig. B.1. We took particular care to fit the continuum as close as possible to the start and end of the $OCN^-$ and CO features to avoid any contamination by the water combination mode at ∼4.5 μm similar to previous works on $OCN^-$ (van Broekhuizen et al. 2005; Boogert et al. 2022).

## 4. Spectral fitting and column densities

### 4.1. $OCN^-$

We fit the $OCN^-$ feature at 4.62 μm in combination with the adjacent CO ice band following the method used in previous studies using higher spectral resolution data (Fig. 2; Pontoppidan et al. 2003; Boogert et al. 2022). The CO ice band is expected to be composed of two Gaussian profiles at 2139.9 $cm^{-1}$ (4.673 μm) and 2143.7 $cm^{-1}$ (4.665 μm) with full width at half maximum (FWHM) of 3.5 $cm^{-1}$ and 3.0 $cm^{-1}$, and one Lorentzian profile at 2136.5 $cm^{-1}$ (4.681 μm) with FWHM of 10.6 $cm^{-1}$. These three components indicate CO in different ice environments. The broad most redshifted Lorentzian profile is expected to be CO mixed with polar species such as $H_2O$ and $CH_3OH$, and is thus referred to as a $CO_{polar}$ component. The Gaussian profile in the middle is expected to be CO in an apolar environment, and is thus referred to as $CO_{apolar}$. The minor shortest wavelength Gaussian component is likely CO mixed with $CO_2$ ice, and is often referred to as $CO_{blue}$ (Tielens et al. 1991; Boogert et al. 2002; Pontoppidan et al. 2003). We opted to include these three components as opposed to a single Gaussian in our fitting. This choice was made after a few tests on the higher spectral resolution data ($R$∼10 000) of Pontoppidan et al. (2003). We first convolved the data used in that study for a few objects to the NIRSpec spectral resolution ($R$∼2700). Next, we applied our fitting procedure to both the data and its convolved version. We found similar fits for the three components to well within 10% which led us to follow the same procedure as Pontoppidan et al. (2003).

The feature at ∼4.6 μm was decomposed into two Gaussian profiles (at 2165.7 $cm^{-1}$, 4.617 μm, with FWHM of 26 $cm^{-1}$ and at 2175.4 $cm^{-1}$, 4.597 μm, with FWHM of 15 $cm^{-1}$) by van Broekhuizen et al. (2005) using the higher spectral resolution VLT data. The major component at 2165.7 $cm^{-1}$ is often firmly associated with $OCN^-$ (van Broekhuizen et al. 2005; Öberg et al. 2011). However, given the lower spectral resolution of JWST, the complexities with the gas-phase lines and their removal from the ∼4.6 μm feature (Sect. 3), we only considered one Gaussian to fit

the data. We note that these issues are less important for the CO band as fewer weaker CO ro-vibrational lines have transitions over the narrower CO ice band. We allowed the single Gaussian parameters for $OCN^-$ to vary freely.

In total, we fitted the 4.5–4.75 μm region with four profiles (one for $OCN^-$ and three for CO) simultaneously using the `curve_fit` function in Python. We fitted the spectra obtained from the spline fitting (i.e., those with gas-phase lines removed). The final fits are presented in Figs. 2 and B.2 (see B.3 for the CO fits) overlaid with the data including gas-phase lines to emphasize the good match. These figures show that $OCN^-$ is detected toward all our objects and the final model (lime green line) closely matches the data. They also show that the $OCN^-$ feature is strong enough to be fitted regardless of the uncertainty associated with the spline fitting.

The comparison of the FWHM and peak position from our single Gaussian profiles with the components considered in van Broekhuizen et al. (2005) is presented in Fig. B.4. For ∼90% of our objects both the peak position and FWHM fall between the range considered by van Broekhuizen et al. (2005) for their two components. However, the FWHM of our Gaussian profiles for two objects (EDJ2009183-A and Per-emb-55-B) are smaller than than 15 $cm^{-1}$ (i.e., FWHM for the minor component considered in van Broekhuizen et al. 2005). This is likely due to the weakness of the $OCN^-$ feature and strong gas-phase emission lines for these two objects in our sample (Fig. B.2).

After the fitting, we calculated the column density of $OCN^-$ and CO components using

$$N = \int \tau_{\tilde{\nu}} d\tilde{\nu}/A, \tag{2}$$

where $\tau_{\tilde{\nu}}$ is the optical depth at wavenumber $\tilde{\nu}$ and $A$ is the band strength. We take the band strengths of CO and $OCN^-$ from the new laboratory measurements of Gerakines et al. (2023) and Gerakines et al. (2025) as $1.1 \times 10^{-17}$ cm molecule$^{-1}$ and $1.5 \times 10^{-16}$ cm molecule$^{-1}$ (Table A.2). It is worth noting that Pontoppidan et al. (2003) introduced an additional factor of 0.71 to be multiplied by $A_{CO}$ when measuring the column density of the middle $CO_{apolar}$ from Eq. (2). This was to take into account grain shape effects in the Rayleigh limit, in which case the band strength of the middle $CO_{apolar}$ component is expected to decrease by 29%. However, in our calculations the same $A$ of $1.1 \times 10^{-17}$ cm molecule$^{-1}$ has been assumed for all three components of CO, and we do not consider this additional factor. In other words, including that factor would increase our column densities of $CO_{apolar}$ by 1.41 (i.e., 1/0.71). Nevertheless, either approach is an assumption and a more detailed study of grain shape and size effects on column densities is needed. Finally, for some objects (B1-b, B1-c, IRAS 2A, L1527, Per-emb-8, Per-emb-22, and Per-emb-33) the bottom of the CO band approaches the noise level in flux scale and thus is not reliable. For those, we only fit the wings of the CO feature to estimate the true optical depth of CO.

We note that the total CO ice column densities for our sample have been measured by Brunken et al. (2024b). We opted to re-measure them, but considering $OCN^-$ contribution to the fits simultaneously because Brunken et al. (2024b) simply integrated the data over the CO absorption feature (∼4.65–4.72 μm). The band strength used for CO in our work is $1.1 \times 10^{-17}$ cm molecule$^{-1}$ from new laboratory experiments (Gerakines et al. 2023), while the one used in Brunken et al. (2024b) from older studies (Gerakines et al. 1995; Bouilloud et al. 2015) was $1.4 \times 10^{-17}$ cm molecule$^{-1}$ (i.e., a factor of 1.27 larger). We report the column densities of $OCN^-$ in Table 1 and report the column densities of different CO components with their sums in Table A.3. The uncertainty in the column densities is on the order of 20%, considering the uncertainty in the fits, data, and continuum subtraction (see the discussion in Appendix A of Brunken et al. 2024b). The band strengths for CO and $OCN^-$ from the new laboratory work have uncertainties that are negligible (∼5%; Gerakines et al. 2023, 2025). We note that the band strengths would change for ices in different ice matrices, but are not expected to change by more than ∼10–20%. Within the uncertainties, our $OCN^-$ column densities for B1-c and IRAS 2A are consistent with those found from the $OCN^-$ transition at 7.6 μm (Chen et al. 2024; Rocha et al. 2024), providing a confirmation for the reliability of both methods. Our total CO column densities agree with those of Brunken et al. (2024b) after correction for the different band strengths used, within ∼15–20% for about half of our objects (i.e., those with minimal contribution from $OCN^-$ to CO or vice versa). However, for the other half, the difference is larger and can reach a factor of ∼1.5. These objects are mostly those with a saturated CO band, where we fit the wings of the CO feature, and thus estimate larger CO column densities than those obtained by direct integration of the observed feature.

**Table 1.** $OCN^-$ ice column densities.

| Source | $OCN^-$ ($\times 10^{16}$ cm$^{-2}$) |
|---|---|
| B1-a-N | 1.3 |
| B1-a-S | 0.8 |
| B1-b | 2.7 |
| B1-c | 15.4 |
| EDJ2009183-A | 0.3 |
| EDJ2009183-B | 0.3 |
| IRAS 2A | 16.8 |
| L1448-mm | 6.5 |
| L1527 | 7.0 |
| Per-emb-8 | 3.9 |
| Per-emb-22 | 8.9 |
| Per-emb-33 | 8.8 |
| Per-emb-35 | 12.5 |
| Per-emb-55-A | 0.6 |
| Per-emb-55-B | 0.2 |
| S68N | 5.5 |
| SMM3 | 5.7 |
| TMC1-W | 1.7 |
| TMC1-E | 2.9 |

**Notes.** The uncertainties in the column densities are estimated as ∼20% originating from the fits and the data, while the uncertainty in the band strength is negligible (at ∼5%; Gerakines et al. 2025).

### *4.2. Complex cyanides and $N_2O$*

#### 4.2.1. NIRSpec range

The absorption bands of complex cyanides and $N_2O$ are relatively weak. The detection of these weaker features are less robust especially for the more line-rich objects. Therefore, we considered each object individually and for this section we only focus on the subset of sources where the CN-stretching absorption feature is detected and does not seem to be an artifact when the spline fitted to the data is compared to the data themselves.

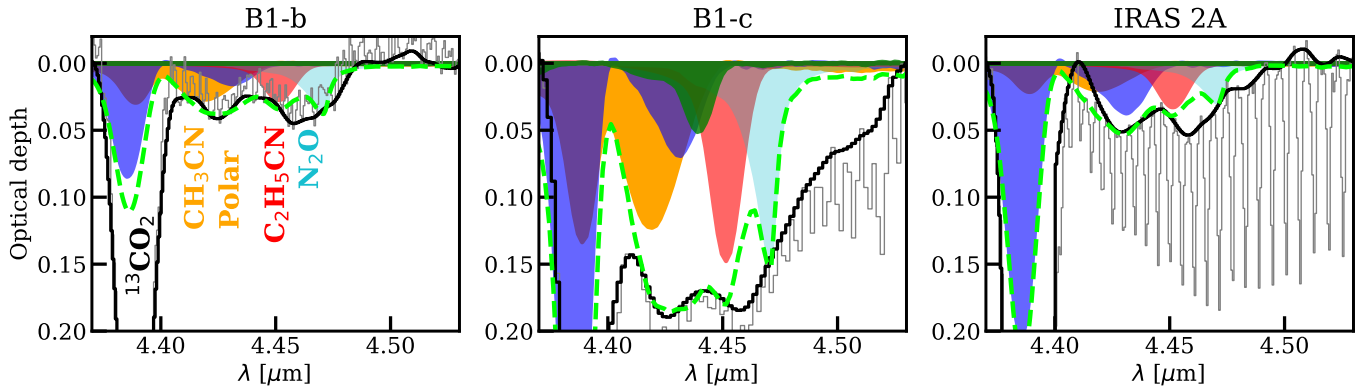


**Fig. 3.** Final fits to the cyanide stretch for objects showing tentative detections of complex cyanides and $N_2O$. The black line shows the spline fitted to the bottom of the gas-phase emission or the top of the gas-phase absorption lines, and the gray line shows the data. Orange and blue show the ice mixtures of $CH_3CN$:$H_2O$:$CO_2$ (1:5:2, 50 K) and $CH_3CN$:$CO_2$ (1:10, 15 K; polar ices); green shows the $CH_3CN$:CO ice mixture (1:10, 80 K; apolar ices); red shows the $C_2H_5CN$ component (50 K); and cyan $N_2O$ (70 K). The total fit is shown as a lime green dashed line.

We fit the CN-stretching band by eye using the same components as Nazari et al. (2024), where the minimum number of components from the available laboratory data was found to fit the CN-stretching band. These components are $CH_3CN$ ice mixtures, $C_2H_5CN$, and $N_2O$. The laboratory spectra for these molecules are taken from Rachid et al. (2022), Moore et al. (2010), and Gerakines & Hudson (2020), respectively. It is worth noting that water has a broad band due to its combination mode at 4.5 μm. However, because of the way that the local continuum is fitted (i.e., as close to the ice features as possible, Fig. 1), the water combination mode is already subtracted before any further fitting to the ice bands. We tested that this is indeed the case for B1-c.

The final fits are shown in Fig. 3. We emphasize that these fits are not unique, but scaling these components differently to fit the data will affect the column densities by less than a factor of ∼2. Moreover, we only claim a tentative detection of $CH_3CN$, $C_2H_5CN$, and $N_2O$, considering the uncertainties that are attributed to the final fits. Another reason for being conservative is that although the current fits presented in Fig. 3 are based on the minimum number of components required from the available laboratory data, we cannot rule out the possibility of laboratory data that are missing and could fit this region with smaller number of components. More specifically, Fig. 3 consistently hints that an unidentified absorption feature is present between the $C_2H_5CN$ and $N_2O$ peaks at ∼4.46 μm. Therefore, that feature may be explained by one component with a smaller contribution from $C_2H_5CN$ and $N_2O$. Potentially, this component could be an ice mixture of $C_2H_5CN$ or $N_2O$ that could easily be shifted from the pure spectra shown here. However, to the best of our knowledge the laboratory spectra of these mixed ices are not yet available. We used Eq. (2) to find the column densities of $CH_3CN$, $C_2H_5CN$, and $N_2O$ which are given in Table 2 and their band strengths in Table A.2. The uncertainty in the column density is dominated by the continuum determination and that of the band strength. We estimate an uncertainty of around 50% on our column densities of $CH_3CN$, $C_2H_5CN$, and $N_2O$.

#### 4.2.2. MIRI range

After the ∼4.5 μm feature, the second-best wavelength range to search for $CH_3CN$, $C_2H_5CN$, and $N_2O$ is ∼6.8–8 μm, which can be used for consistency checks. The ∼6.8–8 μm range is also where many other complex organic molecules have a strong transition (Yang et al. 2022; Rocha et al. 2024; Chen et al. 2024). Therefore, initial modeling of that regime with other molecules is needed (Rayalacheruvu et al. 2025). Thus, here we only consider the two objects in our sample for which this modeling has been done, namely B1-c (Chen et al. 2024) and IRAS 2A (Rocha et al. 2024). Figure B.5 presents the total fit on top of the continuum- and silicate-subtracted spectra from these two papers, where we have added $CH_3CN$, $C_2H_5CN$, and $N_2O$ lab spectra scaled based on our fits to the ∼4.5 μm regime. For IRAS 2A (left panel of Fig. B.5), most new features are small enough such that the total fit remains relatively consistent with the data. However, for B1-c our column densities from the 4.5 μm band are not entirely consistent with the fit at ∼6.8–8 μm (right panel of Fig. B.5). This may be related to $CH_3CN$, $C_2H_5CN$, and $N_2O$ not being responsible for the entire ∼4.5 μm absorption feature. However, $N_2O$ has also been tentatively detected toward the Ced 110 IRS4A protostellar system at 7.75 μm (Rocha et al. 2025). Alternatively, (local) continuum subtraction and silicate subtraction uncertainties in the ∼6.8–8 μm region could play a role. As the cyanide features are relatively weak compared to other COMs studied by Chen et al. (2024) and Rocha et al. (2024), we refrain from claiming a detection for our molecules even after considering the MIRI range.

**Table 2.** Ice column densities of $CH_3CN$, $C_2H_5CN$, and $N_2O$.

| Sources | $N_{CH_3CN}$ (cm$^{-2}$) | $N_{C_2H_5CN}$ (cm$^{-2}$) | $N_{N_2O}$ (cm$^{-2}$) |
|---|---|---|---|
| B1-b | $2.4 \times 10^{17}$ | $8.9 \times 10^{16}$ | $5.6 \times 10^{15}$ |
| B1-c | $1.4 \times 10^{18}$ | $4.8 \times 10^{17}$ | $2.3 \times 10^{16}$ |
| IRAS 2A | $3.8 \times 10^{17}$ | $1.1 \times 10^{17}$ | $4.5 \times 10^{15}$ |

**Notes.** The uncertainties for these species are estimated as 50%, dominated by the continuum fitting and the uncertainty in the band strength.

### *4.3. Silicate and $H_2O$*

We considered the ratios of our $OCN^-$ measurements with respect to $H_2O$ as well as the relation between the column densities and $A_V$ to estimate the formation timeline of $OCN^-$.

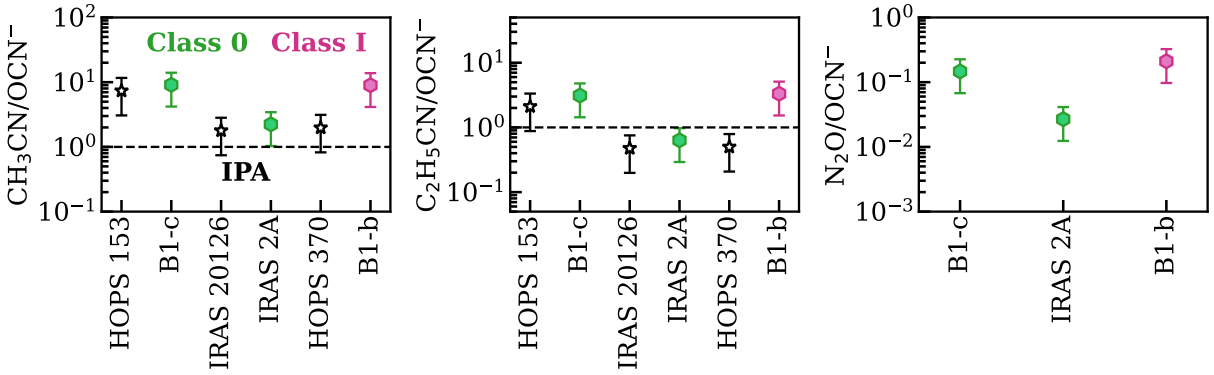


**Fig. 4.** Ice column density ratios of nitrogen-bearing molecules considered. Green represents Class 0 objects and pink Class I objects. The black data points are the results of the IPA JWST program, updated for the $OCN^-$ band strength used here (i.e., ∼15% higher; Nazari et al. 2024). The objects are ordered by their bolometric temperature ($T_{bol}$) from left to right.

Therefore, we measured $A_V$ by fitting the ∼9.8 μm silicate feature and multiplying $\tau_{peak}$ of that feature by 28.6 (based on dense clouds) and 18.5 (based on diffuse clouds) for Class 0 and I objects (Boogert et al. 2013; Madden et al. 2022; van Dishoeck et al. 2025). The reason for this difference is that van Dishoeck et al. (2025) found unreasonably high accretion rates if the same conversion of 28.6 was applied to Class I objects. Therefore, they used the relation found from diffuse clouds (see their Appendix G), which we follow. The silicate at ∼9.8 μm and water absorption at 13.6 μm are fitted together following the same method as used in Rocha et al. (2024) and Chen et al. (2024). Specifically, we first fit a global polynomial continuum to the entire MIRI spectrum of the objects and after subtraction of this continuum, we fit a mixture of synthetic silicates (consisting of small and large pyroxene and olivine grains) to the 9.8 μm band. Next the water at 13.6 μm is fitted. Normally, this method results in reasonable total fits, but in some cases iteration is needed between water and silicate fitting to ensure a good fit. This fitting process is done by hand, using an interactive code that is introduced and explained in detail in Chen et al. (in preparation). Our method does not consider the contribution from carbon, and thus our $A_V$ values may be lower limits. Nevertheless, this effect is not expected to change the values by more than ∼20%.

The water band for most objects could be fitted with a cold (15 K) and warm (150 K) component using the laboratory spectra of Slavicinska et al. (2025). The band strengths for the column density measurement of water are given in Table A.2. We also note that our fits are not unique, and thus it is important to consider the final values as approximate. To better constrain the range of possible values, we varied the continuum and silicate fitting to obtain multiple reasonable fits, and we report the minimum and maximum possible $A_V$ considering those different fits. The final $A_V$ and water column densities represent the middle of that range per object, and are generally in good agreement with those found by Chen et al. (in preparation) within ∼50%. Table A.4 presents the results of this fitting for $A_V$ and water.

### 4.4. NO

Another molecule that we considered in this work is NO. This is stimulated by the detection of NO in the gas phase toward the Class II object Oph-IRS 48 at the location of the ice trap in the disk, where ices are thought to have thermally sublimated (Brunken et al. 2022; Booth et al. 2024). Moreover, $N_2O$ is tentatively detected in our ices (Sect. 4.2) and there might be a chemical connection between $N_2O$ and NO from chemical models of Leemker et al. (2023). As shown in laboratory work by Fulvio et al. (2019), NO has a peak position at 1869 $cm^{-1}$ (or 5.35 μm), which falls in the MIRI range. We thus searched for NO in all of our objects. After spline fitting to remove the gas-phase lines and a local continuum subtraction, five objects showed a tentative absorption feature at 5.35 μm as presented in Fig. B.6 (their MIRI optical depth rms error ranged between $\sim5\times10^{-4}$–$5\times10^{-3}$). Assuming that the entire absorption feature at 5.35 μm is due to NO, we find upper limits of $\sim3\times10^{16}$–$10^{17}$ $cm^{-2}$ for the five objects. In our by-eye fitting, we fixed the FWHM of NO to 20 $cm^{-1}$ based on the NO ice feature that were produced from irradiation of $NO_2$:$N_2O_4$ ice in Fulvio et al. (2019, see their Figs. 6 and 7). The column densities were calculated using Eq. (2) and assuming a band strength of $6.8\times10^{-18}$ cm molecule$^{-1}$ (Stirling et al. 1994; Jamieson et al. 2005; Fulvio et al. 2019). Our calculated $NO/OCN^-$ upper limits are ∼0.2–3. Considering the same objects, the $NO/OCN^-$ upper limits are a factor of ∼1–10 higher than the $N_2O/OCN^-$ ratios and a factor of ∼2–100 lower than those for $CH_3CN/OCN^-$ (Fig. 4). Thus, this indicates that neither $N_2O$ nor NO stores the bulk of nitrogen in ices.

We can also compare our values to the Leemker et al. (2023) predictions for NO in ices to match the gas-phase observations of NO toward Oph-IRS 48. They found that an abundance of $\sim5\times10^{-6}$–$10^{-5}$ with respect to hydrogen ($N_H = 1.6\times10^{22}$ $cm^{-2}$) was needed in the ices. Converting our measured visual extinctions ($A_V$; see Table A.4 and Sect. 4.3) to $N_H$ using $1.37\times10^{21}A_V$ (Evans et al. 2009), we find $N_{NO}/N_H$ abundances of $\sim2\times10^{-7}$–$10^{-6}$, which are around one order of magnitude lower than those required for NO in ices to reproduce the observations of gas-phase NO toward Oph-IRS 48 (Leemker et al. 2023). This might further point to the gas-phase NO being a secondary product of other ice species such as $N_2O$ as discussed in Leemker et al. (2023). No explicit $N_2O$ ice chemical network was included in their models. However, the detected $N_2O$ in our objects have abundances of $\sim2\times10^{-8}$–$10^{-7}$, which are in good agreement with the NO gas-phase abundances toward Oph-IRS 48, making $N_2O$ a likely parent molecule of NO after desorbing from the ices.

### 4.5. Ice ratios

Figure 4 presents the ice column density ratios of $CH_3CN$, $C_2H_5CN$, and $N_2O$ with respect to $OCN^-$. The results of the

cyanide ice analyses from the IPA program are also plotted (Nazari et al. 2024). Generally, there is good agreement between column density ratios of different sources. The column density ratios range within about one order of magnitude for various objects. These constant column density ratios point to similar ice environment of $CH_3CN$, $C_2H_5CN$, and $N_2O$ with $OCN^-$ and may indicate that the complex cyanides form along with $OCN^-$. In Sect. 5 we discuss the formation of $OCN^-$ in detail. Nazari et al. (2024) compared the ice ratios in the IPA sample with the gas-phase data. They found that the ratios were roughly similar between the gas and ice where the differences were associated with various physical and chemical effects. Given the good agreement of our ice results with those from the IPA data, similar conclusions hold.

The ratios of $CH_3CN/OCN^-$ are between ~1–10 which are the largest compared with ratios of $C_2H_5CN$ and $N_2O$ with respect to $OCN^-$. The $C_2H_5CN/OCN^-$ ratios vary between ~0.2–2 and $N_2O/OCN^-$ ratios vary between ~0.01–0.1. Of these three molecules, $CH_3CN$ could be an important nitrogen reservoir given that it could have an ice column density as large as ten times the amount of $OCN^-$, pushing it close to the abundances observed for $NH_3$ in low-mass protostellar ices (Bottinelli et al. 2010; Öberg et al. 2011). Nevertheless, a somewhat larger fraction of nitrogen is likely in salty refractories ($NH_4^+$), as was found by Slavicinska et al. (2025).

The few objects in the IPA program that showed tentative detection of $CH_3CN$ were also those with evidence of ice thermal processing seen as a double-peak feature in the $^{13}CO_2$ band (Brunken et al. 2024a) and those with the highest luminosities. This led Nazari et al. (2024) to conclude that there may be tentative evidence of enhancement of $CH_3CN$ in thermally processed and warmer ices. However, with the larger sample in this work, we find this trend no longer holds. Inspecting the $^{13}CO_2$ bands in our sample as presented in Brunken et al. (2024b, also see our Figs. 1 and B.1), we find objects that do show a (tentative) $CH_3CN$ detection but do not seem to have thermally processed ices (e.g., B1-c) or vice versa (e.g., L1527 and Peremb-35). Therefore, there is no strong evidence of enhancement of $CH_3CN$ in warmer ices from this larger sample.

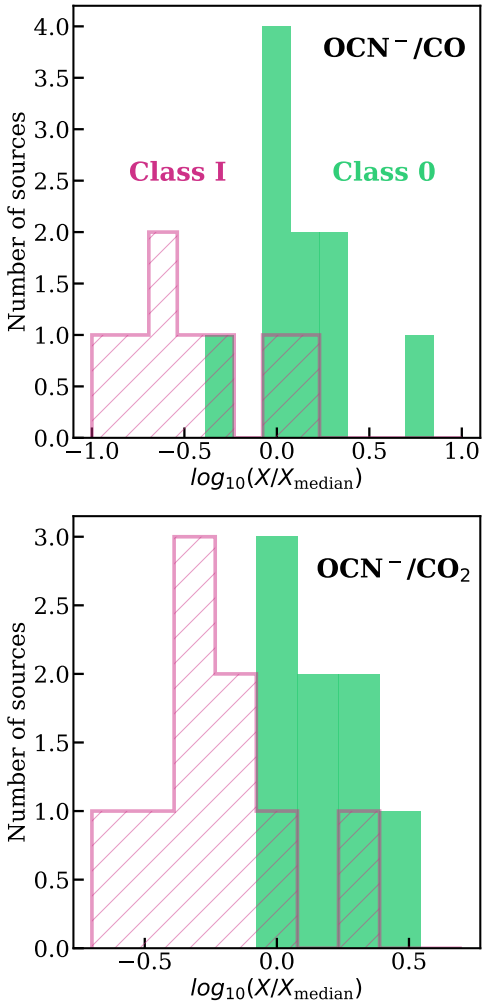


**Fig. 5.** Histogram of Class 0 (smooth green) and I (hatched pink) objects distributed based on $log_{10}(X/X_{median})$, where $X$ is $OCN^-/CO$ in the top panel and $OCN^-/CO_2$ in the bottom panel. The $CO_2$ column densities are taken from Brunken et al. (2024b). The Class 0/I objects have been assumed as Class 0 in this figure. There is a separation between Class 0 and I objects in both $OCN^-/CO$ and $OCN^-/CO_2$.

## 5. $OCN^-$ formation

Previous studies using ground-based telescopes could either study ices of high-mass protostellar systems or bright low-mass systems that were mainly Class I objects (see, e.g., review by Boogert et al. 2015). With JWST we can, for the first time, also study $OCN^-$ in Class 0 sources. Figure 5 presents histograms of our objects divided based on their $OCN^-/CO$ and $OCN^-/CO_2$ ice ratios. This figure interestingly shows a divide between Class 0 and I objects. The Class 0 and those on the border of Class 0/I in general have larger $OCN^-/CO$ and $OCN^-/CO_2$ than late Class Is. This might be related to contribution from the ices of the disk for the more evolved objects. However, to investigate this further detailed radiative transfer models including ices (i.e., similar to those of Sturm et al. 2023 and Bergner et al. 2024 for Class IIs) that consider the evolution from Class 0 to Class I are required, which is outside the scope of this work.

### 5.1. Thermal processing

To assess the effect of heating on formation of $OCN^-$, Fig. 6 presents the column density ratios of $OCN^-$ with respect to $CO_2$. The sources are divided into two groups based on the shape of their 15.2 μm $CO_2$ absorption band. The objects with a double-peak morphology are shown in red and those with a single-peak morphology are shown in blue. Those with a double-peak $CO_2$ feature are thought to indicate thermally processed ices (Pontoppidan et al. 2008; Brunken et al. 2025). Figure 6 shows that objects with thermally processed ices (double-peak $CO_2$ morphology) statistically have a factor of ~2–3 larger $OCN^-/CO_2$ than those ices without thermal processing. The same general trend holds for $OCN^-/H_2O$ ratios toward our objects even though that is less certain considering the complexities in water column density measurements (Sect. 4.3). Therefore, the increased $OCN^-/CO_2$ ratios are likely not caused by $CO_2$ sublimation for the objects with more thermally processed ices.

This factor of ~2–3 increase is in excellent agreement with the results from van Broekhuizen et al. (2004) laboratory experiments. They found that $OCN^-$ can form more efficiently at higher temperatures where the difference between $OCN^-$ abundance at 20–40 K and 120–140 K was a factor of ~2–3. They found that UV processing can also enhance the formation of

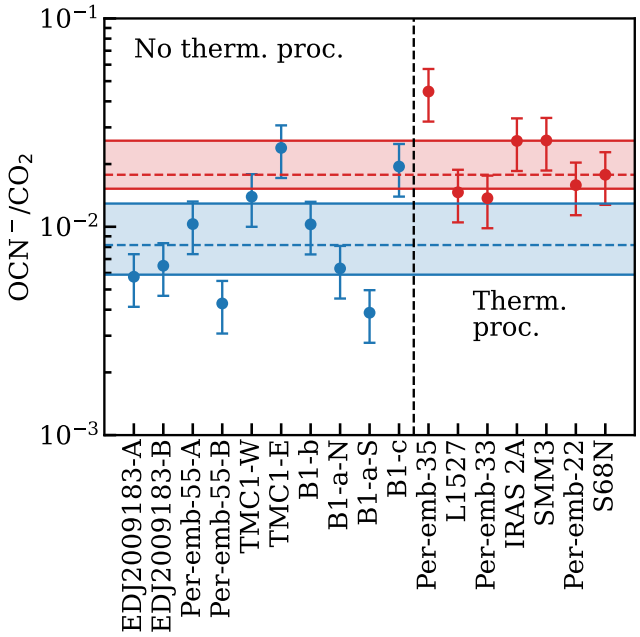


**Fig. 6.** Effect of heating on the $OCN^-/CO_2$ ratio. The objects are divided into two groups based on the shape of the $CO_2$ band. Those with double-peaked $CO_2$ are shown in red (thermally processed ices), while those with a single-peaked $CO_2$ are shown in blue (no thermal processing). The dashed lines show the median of each group and the shaded areas show the range where the data fall between the upper and lower quartiles. Ice heating can increase $OCN^-$ formation by only a factor of ~2–3.

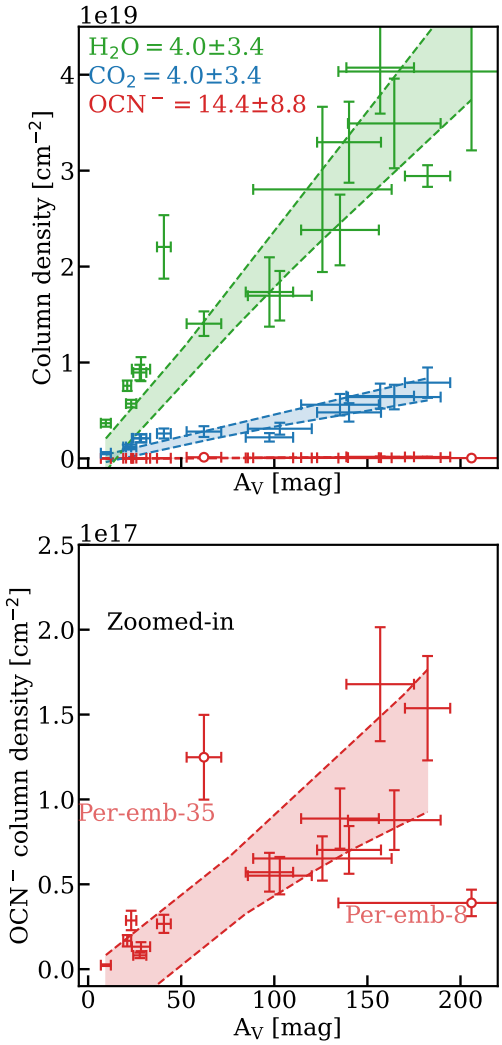


**Fig. 7.** Relation between $A_V$ and column densities of $H_2O$ (green), $CO_2$ (blue), and $OCN^-$ (red). The lower panel shows a zoomed-in version of the upper panel for $OCN^-$. The two data points of $OCN^-$ shown with a white marker are omitted when fitting the trend. The x-intercept of each molecule is printed in its respective color. The $CO_2$ column densities are from Brunken et al. (2024b).

$OCN^-$, but that this required a much larger UV fluence in the laboratory than experienced by grains in molecular clouds. Based on those results and Fig. 6, we conclude that simply detecting $OCN^-$ is not a diagnostic of energetic processing of ices and the effect of heating on $OCN^-$ enhancement is only a factor of ~2–3 across Class 0 and I objects.

### 5.2. Formation timeline with respect to CO, $CO_2$, and $H_2O$

It has been suggested that $OCN^-$ forms through the acid-base reaction of HNCO and $NH_3$, while HNCO itself can form via reactions of NH and $NH_2$ with CO ice (Fedoseev et al. 2016; Ligterink et al. 2018). Because of the high sublimation temperature of salts (~200 K in temperature programmed desorption experiments; Ligterink et al. 2018) $OCN^-$ can survive the later ice processing in a polar environment (van Broekhuizen et al. 2005; Öberg et al. 2011; Boogert et al. 2022). In this section we investigate this further by considering the relation between $OCN^-$ column densities and the visual extinction ($A_V$) of our objects. In Boogert et al. (2015) the x-intercepts of column densities of $H_2O$, $CO_2$, and CO in molecular clouds as a function of $A_V$ are suggested to indicate the formation order of these molecules. Here, we attempt to examine the same relation for $OCN^-$, $H_2O$, and $CO_2$ in our objects, keeping in mind that in our case heating might affect the linearity of the relation and that a large extrapolation is needed to find the x-intercepts due to the large visual extinction of protostellar objects.

Figure 7 presents column densities of $H_2O$, $CO_2$, and $OCN^-$ as a function of $A_V$. We find that even up to $A_V$~200 mag, $H_2O$ and $CO_2$ show a linear relationship with $A_V$ and this relationship still holds despite the warmer environment of the protostellar systems. The $OCN^-$ column densities also show a linear relationship, even though two objects are clear outliers. These two objects are Per-emb-8 and Per-emb-35. The former has an uncertain silicate fitting because the 9.8 μm band reaches the noise limit, and therefore the ~18 μm silicate band was used instead. The latter has a particularly prominent double-peak $CO_2$ feature (Brunken et al. 2025), and thus its ices are strongly thermally processed (also see Fig. 6). Therefore, we omitted these two sources when fitting the relation for $OCN^-$ as a function of $A_V$.

The *x*-intercept values in Fig. 7 have large error bars. This is because most of our objects have $A_V$ values that are larger than ~40, and thus extrapolation was needed. As a result, robust conclusions on the formation timelines of these molecules are difficult to make with this dataset and clouds with lower $A_V$ (e.g., those of Smith et al. 2025) are required for such a conclusion. Nevertheless, the *x*-intercept of $H_2O$ and $CO_2$ are in agreement within the error bars with the ~2–3 mag found toward clouds for these two molecules (Boogert et al. 2015). Moreover, the $OCN^-$ x-intercept range goes up to values that are somewhat larger than the range found for the other two molecules, but all three still agree within the uncertainties. To investigate this

further, we also considered the relation between $CO/H_2O$ and $CO_2/H_2O$ with $OCN^-/H_2O$ in Appendix C. We did not find any relation between $CO_2/H_2O$ and $OCN^-/H_2O$. This lack of relation together with Fig. 7 are in agreement with the previous studies that concluded that $OCN^-$ may form later than $H_2O$ and $CO_2$ in CO-rich ices.

## 6. Conclusions

In this work, we analyzed the absorption bands in the ~4.4–4.7 μm region for the JOYS+ low-mass protostellar systems. This sample includes Class 0 and Class I objects and extends the pre-JWST results to include objects with lower $T_{bol}$. Our main conclusions are summarized below:

- We detect $OCN^-$ in ices of all 19 sources. The objects showing a double-peak $CO_2$ (15.2 μm), a sign of thermal processing, have a factor of ~2–3 higher $OCN^-/CO_2$ (Fig. 6). Therefore, higher temperatures can enhance $OCN^-$ formation, but only moderately, and detection by itself is not an indicator of thermal processing;
- The $OCN^-$, $H_2O$, and $CO_2$ relations with $A_V$ (Fig. 7) and lack of relation between $CO_2/H_2O$ and $OCN^-/H_2O$ tentatively point to formation of $OCN^-$ after $H_2O$ and $CO_2$ have already formed in agreement with previous studies;
- We find a separation between Class 0 and I objects when considering their $OCN^-/CO$ and $OCN^-/CO_2$ ratios, with Class 0 systems generally showing larger values. Understanding the origin of this division requires further radiative transfer modeling of Class 0 and Class I objects;
- We also tentatively detect $CH_3CN$, $C_2H_5CN$, and $N_2O$ in ices of three objects (B1-b, B1-c, and IRAS 2A). The column density ratios of $CH_3CN$, $C_2H_5CN$, and $N_2O$ with respect to $OCN^-$ are relatively constant (Fig. 4), which suggests that they likely formed in a similar ice environment to $OCN^-$. Out of these three, $CH_3CN$ shows the highest ratios with respect to $OCN^-$ in the range ~1–10 and could potentially be an important nitrogen budget in ices;
- We find upper limit abundances of $\sim 2 \times 10^{-7}$–$10^{-6}$ for NO toward five of our objects. These are around one order of magnitude lower than what is expected in ices of the Oph-IRS 48 to explain the gas-phase detection of NO. This likely points to the observed gas-phase NO being a secondary product of another ice species such as $N_2O$. Given similar ice abundances of $N_2O$ toward our objects with the NO gas-phase abundance toward Oph-IRS 48, this scenario is likely.

In this paper, we showed that the JWST sensitivity is key for the analysis of ice features toward faint objects with the highest ice column densities. Moreover, the spectral coverage of the entire 4.3–4.8 μm region is key for continuum determination and robust column density estimation of $OCN^-$. A larger sample with $CO_2$, $OCN^-$, and $H_2O$ measurements are required to further confirm the conclusions made here. This would be particularly useful if measured toward pre-stellar cores. As for the complex cyanides and $N_2O$, future deeper observations (similar to that of B1-c in this work), preferably toward objects with weak gas-phase lines, and laboratory data for ice mixtures of $C_2H_5CN$ and $N_2O$ are needed to make more meaningful deductions.

*Acknowledgements.* We thank K. Pontoppidan and H. Beuther for their insightful comments. This work is based on observations made with the NASA/ESA/CSA *James Webb* Space Telescope. The data were obtained from the Mikulski Archive for Space Telescopes at the Space Telescope Science Institute, which is operated by the Association of Universities for Research in Astronomy, Inc., under NASA contract NAS 5-03127 for JWST. These observations are associated with programs #1186, #1236, #1290, and #1960. P.N. acknowledges support from the ESO Fellowship and IAU Gruber Foundation Fellowship programs. Astrochemistry at Leiden is supported by funding from the European Research Council (ERC) under the European Union's Horizon 2020 research and innovation program (grant agreement No. 101019751 MOLDISK), the Netherlands Research School for Astronomy (NOVA), and the Danish National Research Foundation through the Center of Excellence 'InterCat' (grant agreement No. DNRF150). V.J.M.L.G. acknowledges support by the Spanish program Unidad de Excelencia María de Maeztu CEX2020-001058-M, financed by MCIN/AEI/10.13039/501100011033, and by the MaX-CSIC Excellence Award MaX4-SOMMA-ICE. V.J.M.L.G. acknowledges support by the European Research Council (ERC) under the European Union's Horizon 2020 research and innovation program (grant agreement No. 101098309 – PEBBLES). A.C.G. acknowledges support from PRIN-MUR 2022 20228JPA3A "The path to star and planet formation in the JWST era (PATH)" funded by NextGeneration EU and by INAF-GoG 2022 "NIR-dark Accretion Outbursts in Massive Young stellar objects (NAOMY)" and Large Grant INAF 2022 "YSOs Outflows, Disks and Accretion: toward a global framework for the evolution of planet forming systems (YODA)".

## References

Argyriou, I., Glasse, A., Law, D. R., et al. 2023, A&A, 675, A111
Bardyn, A., Baklouti, D., Cottin, H., et al. 2017, MNRAS, 469, S712
Bergner, J. B., Sturm, J. A., Piacentino, E. L., et al. 2024, ApJ, 975, 166
Beuther, H., van Dishoeck, E. F., Tychoniec, L., et al. 2023, A&A, 673, A121
Böker, T., Arribas, S., Lützgendorf, N., et al. 2022, A&A, 661, A82
Boogert, A. C. A., Blake, G. A., & Tielens, A. G. G. M. 2002, ApJ, 577, 271
Boogert, A. C. A., Pontoppidan, K. M., Knez, C., et al. 2008, ApJ, 678, 985
Boogert, A. C. A., Chiar, J. E., Knez, C., et al. 2013, ApJ, 777, 73
Boogert, A. C. A., Gerakines, P. A., & Whittet, D. C. B. 2015, ARA&A, 53, 541
Boogert, A. C. A., Brewer, K., Brittain, A., & Emerson, K. S. 2022, ApJ, 941, 32
Booth, A. S., Temmink, M., van Dishoeck, E. F., et al. 2024, AJ, 167, 165
Bottinelli, S., Boogert, A. C. A., Bouwman, J., et al. 2010, ApJ, 718, 1100
Bouilloud, M., Fray, N., Bénilan, Y., et al. 2015, MNRAS, 451, 2145
Brunken, N. G. C., Booth, A. S., Leemker, M., et al. 2022, A&A, 659, A29
Brunken, N. G. C., Rocha, W. R. M., van Dishoeck, E. F., et al. 2024a, A&A, 685, A27
Brunken, N. G. C., van Dishoeck, E. F., Slavicinska, K., et al. 2024b, A&A, 692, A163
Brunken, N. G. C., Boogert, A. C. A., van Dishoeck, E. F., et al. 2025, ACS Earth Space Chem., 9, 1992
Calcutt, H., Jørgensen, J. K., Müller, H. S. P., et al. 2018, A&A, 616, A90
Caratti o Garatti, A., Ray, T. P., Kavanagh, P. J., et al. 2024, A&A, 691, A134
Chahine, L., López-Sepulcre, A., Neri, R., et al. 2022, A&A, 657, A78
Chen, Y., Rocha, W. R. M., van Dishoeck, E. F., et al. 2024, A&A, 690, A205
Erb, D. 2024, pybaselines: A Python library of algorithms for the baseline correction of experimental data
Evans, Neal J., I., Dunham, M. M., Jørgensen, J. K., et al. 2009, ApJS, 181, 321
Federman, S. A., Megeath, S. T., Rubinstein, A. E., et al. 2024, ApJ, 966, 41
Fedoseev, G., Chuang, K. J., van Dishoeck, E. F., Ioppolo, S., & Linnartz, H. 2016, MNRAS, 460, 4297
Francis, L., van Gelder, M. L., van Dishoeck, E. F., et al. 2024, A&A, 683, A249
Fray, N., Bardyn, A., Cottin, H., et al. 2016, Nature, 538, 72
Fulvio, D., Baratta, G. A., Sivaraman, B., et al. 2019, MNRAS, 483, 381
Gardner, J. P., Mather, J. C., Abbott, R., et al. 2023, PASP, 135, 068001
Garrod, R. T., Jin, M., Matis, K. A., et al. 2022, ApJS, 259, 1
Gerakines, P. A., & Hudson, R. L. 2020, ApJ, 901, 52
Gerakines, P. A., Schutte, W. A., Greenberg, J. M., & van Dishoeck, E. F. 1995, A&A, 296, 810
Gerakines, P. A., Materese, C. K., & Hudson, R. L. 2023, MNRAS, 522, 3145
Gerakines, P. A., Materese, C. K., & Hudson, R. L. 2025, MNRAS, 537, 2918
Gibb, E. L., Whittet, D. C. B., Schutte, W. A., et al. 2000, ApJ, 536, 347
Gibb, E. L., Whittet, D. C. B., Boogert, A. C. A., & Tielens, A. G. G. M. 2004, ApJS, 151, 35
Gieser, C., Beuther, H., van Dishoeck, E. F., et al. 2023, A&A, 679, A108
Herbst, E. 1980, ApJ, 237, 462
Huntress, W. T. J., & Mitchell, G. F. 1979, ApJ, 231, 456
Jakobsen, P., Ferruit, P., Alves de Oliveira, C., et al. 2022, A&A, 661, A80
Jamieson, C. S., Bennett, C. J., Mebel, A. M., & Kaiser, R. I. 2005, ApJ, 624, 436
Le Gouellec, V. J. M., Lew, B. W. P., Greene, T. P., et al. 2025, ApJ, 985, 225
Leemker, M., Booth, A. S., van Dishoeck, E. F., et al. 2023, A&A, 673, A7
Ligterink, N. F. W., Terwisscha van Scheltinga, J., Taquet, V., et al. 2018, MNRAS, 480, 3628

Madden, M. C. L., Boogert, A. C. A., Chiar, J. E., et al. 2022, ApJ, 930, 2
Mastrapa, R. M., Sandford, S. A., Roush, T. L., Cruikshank, D. P., & Dalle Ore, C. M. 2009, ApJ, 701, 1347
McClure, M. K., Rocha, W. R. M., Pontoppidan, K. M., et al. 2023, Nat. Astron., 7, 431
Moore, M. H., Ferrante, R. F., Moore, W. J., & Hudson, R. 2010, ApJS, 191, 96
Narang, M., Manoj, P., Tyagi, H., et al. 2024, ApJ, 962, L16
Nazari, P., van Gelder, M. L., van Dishoeck, E. F., et al. 2021, A&A, 650, A150
Nazari, P., Meijerhof, J. D., van Gelder, M. L., et al. 2022, A&A, 668, A109
Nazari, P., Tabone, B., van't Hoff, M. L. R., Jørgensen, J. K., & van Dishoeck, E. F. 2023, ApJ, 951, L38
Nazari, P., Rocha, W. R. M., Rubinstein, A. E., et al. 2024, A&A, 686, A71
Neufeld, D. A., Manoj, P., Tyagi, H., et al. 2024, ApJ, 966, L22
Öberg, K. I., Boogert, A. C. A., Pontoppidan, K. M., et al. 2011, ApJ, 740, 109
Pontoppidan, K. M., Fraser, H. J., Dartois, E., et al. 2003, A&A, 408, 981
Pontoppidan, K. M., Boogert, A. C. A., Fraser, H. J., et al. 2008, ApJ, 678, 1005
Rachid, M. G., Rocha, W. R. M., & Linnartz, H. 2022, A&A, 665, A89
Ray, T. P., McCaughrean, M. J., Caratti o Garatti, A., et al. 2023, Nature, 622, 48
Rayalacheruvu, P., Majumdar, L., Rocha, W. R. M., et al. 2025, ApJS, 281, 51
Rocha, W. R. M., Perotti, G., Kristensen, L. E., & Jørgensen, J. K. 2021, A&A, 654, A158
Rocha, W. R. M., van Dishoeck, E. F., Ressler, M. E., et al. 2024, A&A, 683, A124
Rocha, W. R. M., McClure, M. K., Sturm, J. A., et al. 2025, A&A, 693, A288
Rubin, M., Altwegg, K., Balsiger, H., et al. 2019, MNRAS, 489, 594
Rubinstein, A. E., Evans, N. J., Tyagi, H., et al. 2024, ApJ, 974, 112
Salyk, C., Yang, Y.-L., Pontoppidan, K. M., et al. 2024, ApJ, 974, 97
Schutte, W. A., Boogert, A. C. A., Tielens, A. G. G. M., et al. 1999, A&A, 343, 966
Schutte, W. A., & Khanna, R. K. 2003, A&A, 398, 1049
Slavicinska, K., van Dishoeck, E. F., Tychoniec, Ł., et al. 2024, A&A, 688, A29
Slavicinska, K., Boogert, A. C. A., Tychoniec, Ł., et al. 2025, A&A, 693, A146
Smith, Z. L., Dickinson, H. J., Fraser, H. J., et al. 2025, Nat. Astron., 9, 883
Stirling, A., Pápai, I., Mink, J., & Salahub, D. R. 1994, J. Chem. Phys., 100, 2910
Sturm, J. A., McClure, M. K., Bergner, J. B., et al. 2023, A&A, 677, A18
Terwisscha van Scheltinga, J., Marcandalli, G., McClure, M. K., Hogerheijde, M. R., & Linnartz, H. 2021, A&A, 651, A95
Tielens, A. G. G. M., Tokunaga, A. T., Geballe, T. R., & Baas, F. 1991, ApJ, 381, 181
Tyagi, H., Manoj, P., Narang, M., et al. 2025, ApJ, 983, 110
Tychoniec, Ł., van Gelder, M. L., van Dishoeck, E. F., et al. 2024, A&A, 687, A36
van Broekhuizen, F. A., Keane, J. V., & Schutte, W. A. 2004, A&A, 415, 425
van Broekhuizen, F. A., Pontoppidan, K. M., Fraser, H. J., & van Dishoeck, E. F. 2005, A&A, 441, 249
van Dishoeck, E. F., Tychoniec, Ł., Rocha, W. R. M., et al. 2025, A&A, 699, A361
van Gelder, M. L., Francis, L., van Dishoeck, E. F., et al. 2024a, A&A, 692, A197
van Gelder, M. L., Ressler, M. E., van Dishoeck, E. F., et al. 2024b, A&A, 682, A78
Walsh, C., Millar, T. J., Nomura, H., et al. 2014, A&A, 563, A33
Wilson, T. L., & Rood, R. 1994, ARA&A, 32, 191
Wright, G. S., Rieke, G. H., Glasse, A., et al. 2023, PASP, 135, 048003
Yang, Y.-L., Sakai, N., Zhang, Y., et al. 2021, ApJ, 910, 20
Yang, Y.-L., Green, J. D., Pontoppidan, K. M., et al. 2022, ApJ, 941, L13

Table A.1: Spectral extraction positions and source properties.

| Source | R.A. [hh:mm:ss] | Decl. [dd:mm:ss] | Class | Optical depth rms error |
|---|---|---|---|---|
| B1-a-N | 03:33:16.693 | 31:07:55.28 | I | $1.2 \times 10^{-4}$ |
| B1-a-S | 03:33:16.677 | 31:07:54.98 | I | $1.9 \times 10^{-4}$ |
| B1-b | 03:33:20.334 | 31:07:21.64 | I | $3.9 \times 10^{-4}$ |
| B1-c | 03:33:17.893 | 31:09:31.90 | 0 | $3.4 \times 10^{-3}$ |
| EDJ2009183-A | 03:28:59.304 | 31:15:48.48 | I | $5.7 \times 10^{-5}$ |
| EDJ2009183-B | 03:28:59.382 | 31:15:48.48 | I | $2.6 \times 10^{-4}$ |
| IRAS 2A | 03:28:55.574 | 31:14:36.90 | 0 | $1.1 \times 10^{-3}$ |
| L1448-mm | 03:25:38.868 | 30:44:05.66 | 0 | $5.2 \times 10^{-3}$ |
| L1527 | 04:39:53.905 | 26:03:09.69 | 0/I | $5.3 \times 10^{-4}$ |
| Per-emb-8 | 03:44:43.990 | 32:01:35.59 | 0 | $1.2 \times 10^{-3}$ |
| Per-emb-22 | 03:25:22.351 | 30:45:13.18 | 0 | $2.5 \times 10^{-3}$ |
| Per-emb-33 | 03:25:36.316 | 30:45:14.92 | 0 | $1.4 \times 10^{-2}$ |
| Per-emb-35 | 03:28:37.093 | 31:13:30.85 | 0/I | $2.5 \times 10^{-4}$ |
| Per-emb-55-A | 03:44:43.293 | 32:01:31.33 | I | $1.9 \times 10^{-4}$ |
| Per-emb-55-B | 03:44:43.332 | 32:01:31.73 | I | $1.2 \times 10^{-4}$ |
| S68N | 18:29:48.140 | 01:16:44.58 | 0 | $2.6 \times 10^{-3}$ |
| SMM3 | 18:29:59.308 | 01:14:00.58 | 0 | $3.5 \times 10^{-3}$ |
| TMC1-W | 04:41:12.685 | 25:46:34.42 | I | $7.7 \times 10^{-5}$ |
| TMC1-E | 04:41:12.729 | 25:46:34.52 | I | $7.6 \times 10^{-4}$ |

**Notes.** The second and third columns present the right ascension and declination of the aperture center from the NIRSpec cubes used to extract the spectra (i.e., the peak continuum position at 5.251 μm).

## Appendix A: Additional tables

The properties of our objects, the position of spectral extraction, and the rms error on the spectra are given in Table. A.1. The band strengths for the molecules considered here are presented in Table A.2. The column densities of different components of CO are given in Table A.3. It is worth noting that even though, Boogert et al. (2002) multiplied the band strength of the middle $CO_{apolar}$ component by an additional factor of 1.1 to correct for grain shape effects, Boogert et al. (2015), similar to our work, did not include any additional factors for correction of grain shape effects when calculating the middle $CO_{apolar}$ component column density. In other words, they used the formula $3.5\tau_{max}/(1.1 \times 10^{-17})$, where the denominator is the CO band strength from Gerakines et al. (1995). In our work, we consistently do not use any correction for the band strength of $CO_{apolar}$ component, both for our measurements and those calculated from the fit parameters given in Pontoppidan et al. (2003) when comparing with the literature values in Fig. C.1. The measured $A_V$ and $H_2O$ column densities are given in Table A.4.

## Appendix B: Additional plots

Figure B.1 presents the spline and local continuum fitting for the sample. Figure B.2 presents the fits to the $OCN^-$ and CO features combined. This is the continuation of Fig. 2 in the main text. Figure B.3 presents the same but zooming in on the CO ice band. Figure B.4 compares the fitted peak positions and FWHMs to the $OCN^-$ ice band with those of suggested by van Broekhuizen et al. (2005) with their higher spectral resolution data. Figure B.5 presents our fits based on the NIRSpec range on top of the total models found by Rocha et al. (2024) and Chen et al. (2024) for IRAS 2A and B1-c in the MIRI range. Figure B.6 presents the upper limit fits for NO for objects with a tentative absorption feature at ~5.35 μm.

Table A.2: Band strengths.

| Ice species | $A$ (cm molecule$^{-1}$) | Mode |
|---|---|---|
| $CH_3CN$:$CO_2$ | $1.5 \times 10^{-18}$ | C-N stretching |
| $CH_3CN$:CO | $1.5 \times 10^{-18}$ | C-N stretching |
| $CH_3CN$:$H_2O$:$CO_2$ | $3.3 \times 10^{-18}$ | C-N stretching |
| $C_2H_5CN$ | $2.9 \times 10^{-18}$ | C-N stretching |
| $OCN^-$ | $1.5 \times 10^{-16}$ | C-N stretching |
| CO | $1.1 \times 10^{-17}$ | C-O stretching |
| $N_2O$ | $5.7 \times 10^{-17}$ | N-N stretching |
| NO | $6.8 \times 10^{-18}$ | N-O stretching |
| $H_2O$ (15 K) | $2.5 \times 10^{-17}$ | libration |
| $H_2O$ (150 K) | $3 \times 10^{-17}$ | libration |

**Notes.** Band strengths are taken from Rachid et al. (2022) and Gerakines et al. (2025) for $CH_3CN$ mixtures (at 15 K) and $OCN^-$ (at 10 K), respectively. The band strength for CO (at 10 K) is taken from Gerakines et al. (2023). For $C_2H_5CN$ we use the value calculated in Nazari et al. (2024). The band strengths for $N_2O$ and NO are from Gerakines & Hudson (2020) and Fulvio et al. (2019). For the cold and warm water components the band strengths are given in Mastrapa et al. (2009).

## Appendix C: Column densities normalized by $H_2O$

Another clue on formation of $OCN^-$ may be found by considering the relation between column densities of CO and $CO_2$ as a function of $OCN^-$, all normalized by $H_2O$ column densities. Figure C.1 shows these relations. We also added some of the previous literature data to Fig. C.1, where we have considered a 30% uncertainty for non-JWST data points. This is generally larger than what is reported in the original papers and is because those works mainly consider the uncertainty in the fits which are quite small, while the uncertainty in the pre-JWST fluxes are larger which should be reflected in the errorbars. The band strength for all components of CO is assumed as $1.1 \times 10^{-17}$ cm molecule$^{-1}$ for our measurements and is corrected to $1.1 \times 10^{-17}$ cm molecule$^{-1}$ for the literature values to be consistent.

Figure C.1 shows that there is no relation between $OCN^-/H_2O$ and $CO_2/H_2O$ consistent with later formation of $OCN^-$. On the other hand, the relation with $CO/H_2O$ seems more complicated. Considering all objects, $CO/H_2O$ does not seem to have any correlation with $OCN^-/H_2O$. However, excluding the two high-mass objects with the highest $CO/H_2O$ points to a negative correlation where objects with more $OCN^-/H_2O$ are those with less $CO/H_2O$. In Sect. 5.1 we discussed the effect of heating on $OCN^-$ formation. Because high-mass star-forming regions likely have higher temperatures the larger $OCN^-/H_2O$ in Fig. C.1 for the high-mass objects may be due to increase of $OCN^-$ in those warmer regions.

Table A.3: CO ice column densities.

| Source | $CO_{polar}$ [$\times 10^{17}$ cm$^{-2}$] | $CO_{apolar}$ [$\times 10^{17}$ cm$^{-2}$] | $CO_{blue}$ [$\times 10^{16}$ cm$^{-2}$] | Total [$\times 10^{18}$ cm$^{-2}$] |
|---|---|---|---|---|
| B1-a-N | 6.4 | 10.0 | 19.0 | 1.8 |
| B1-a-S | 5.6 | 8.7 | 17.2 | 1.6 |
| B1-b | 36.1 | 33.5 | 26.4 | 7.2 |
| B1-c | 70.5 | 22.4 | 60.8 | 9.9 |
| EDJ2009183-A | 5.7 | 7.6 | 11.6 | 1.4 |
| EDJ2009183-B | 5.1 | 7.3 | 10.9 | 1.4 |
| IRAS 2A | 35.4 | 19.3 | 27.6 | 5.7 |
| L1448-mm | 25.1 | 7.5 | 21.1 | 3.5 |
| L1527 | 26.5 | 14.3 | 14.8 | 4.2 |
| Per-emb-8 | 38.3 | 12.5 | 26.5 | 5.3 |
| Per-emb-22 | 37.0 | 18.7 | 22.6 | 5.8 |
| Per-emb-33 | 50.8 | 14.7 | 37.6 | 6.9 |
| Per-emb-35 | 13.7 | 1.9 | 4.7 | 1.6 |
| Per-emb-55-A | 5.1 | 11.3 | 3.4 | 1.7 |
| Per-emb-55-B | 5.9 | 10.8 | 2.9 | 1.7 |
| S68N | 17.6 | 8.8 | 19.1 | 2.8 |
| SMM3 | 16.2 | 3.5 | 8.4 | 2.0 |
| TMC1-W | 7.1 | 2.8 | 11.5 | 1.1 |
| TMC1-E | 8.2 | 3.4 | 14.6 | 1.3 |

**Notes.** The uncertainties in the column densities from the fit and the data are estimated as ~20%, while the band strength uncertainties are negligible (~5%; Gerakines et al. 2023).

Table A.4: Results of the silicate and water libration mode fitting.

| Source | $\tau_{peak}$ | $A_V$ [mag] | $H_2O$ [$\times 10^{18}$ cm$^{-2}$] |
|---|---|---|---|
| B1-a-N | 1.5 ± 0.3 | 28 ± 5 | ~9.3 |
| B1-a-S | 1.5 ± 0.2 | 28 ± 4 | ~9.0 |
| B1-b | 2.2 ± 0.2 | 41 ± 4 | ~22.0 |
| B1-c | 6.4 ± 0.4 | 182 ± 12 | ~29.4 |
| IRAS 2A | 5.5 ± 0.6 | 157 ± 18 | ~40.7 |
| L1448-mm | 4.4 ± 1.3 | 126 ± 37 | ~28.0 |
| L1527 | 4.9 ± 0.6 | 140 ± 17 | ~33.0 |
| Per-emb-8 | 7.2 ± 2.5 | 206 ± 71 | ~40.3 |
| Per-emb-22 | 4.7 ± 0.7 | 135 ± 21 | ~23.8 |
| Per-emb-33 | 5.8 ± 0.9 | 164 ± 25 | ~34.9 |
| Per-emb-35 | 2.2 ± 0.3 | 62 ± 9 | ~14.0 |
| Per-emb-55-B | 0.5 ± 0.1 | 10 ± 3 | ~3.7 |
| S68N | 3.6 ± 0.6 | 103 ± 17 | ~17.0 |
| SMM3 | 3.4 ± 0.4 | 97 ± 13 | ~17.4 |
| TMC1-W | 1.1 ± 0.1 | 21 ± 2 | ~7.6 |
| TMC1-E | 1.2 ± 0.1 | 23 ± 3 | ~5.7 |

**Notes.** $A_V$ is calculated using the bottom of the silicate feature at ~9.8 μm ($\tau_{peak}$) and multiplying that by 28.6 and 18.5 for Class 0 and I objects, respectively (see Boogert et al. 2013 and Appendix G of van Dishoeck et al. 2025). The Class 0/I objects are assumed as Class 0 for this conversion.

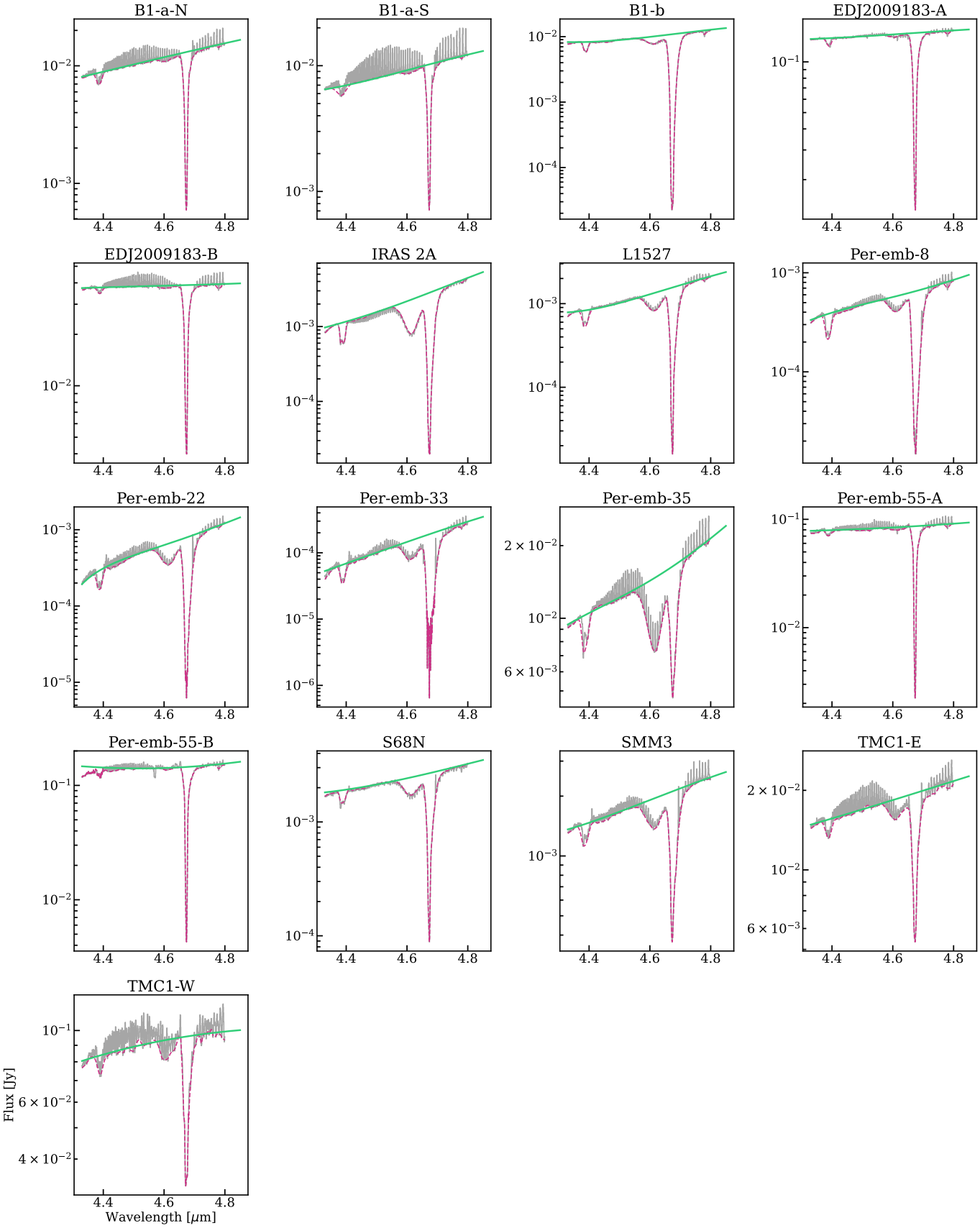


Fig. B.1: Same as Fig. 1 but for the rest of our sample.

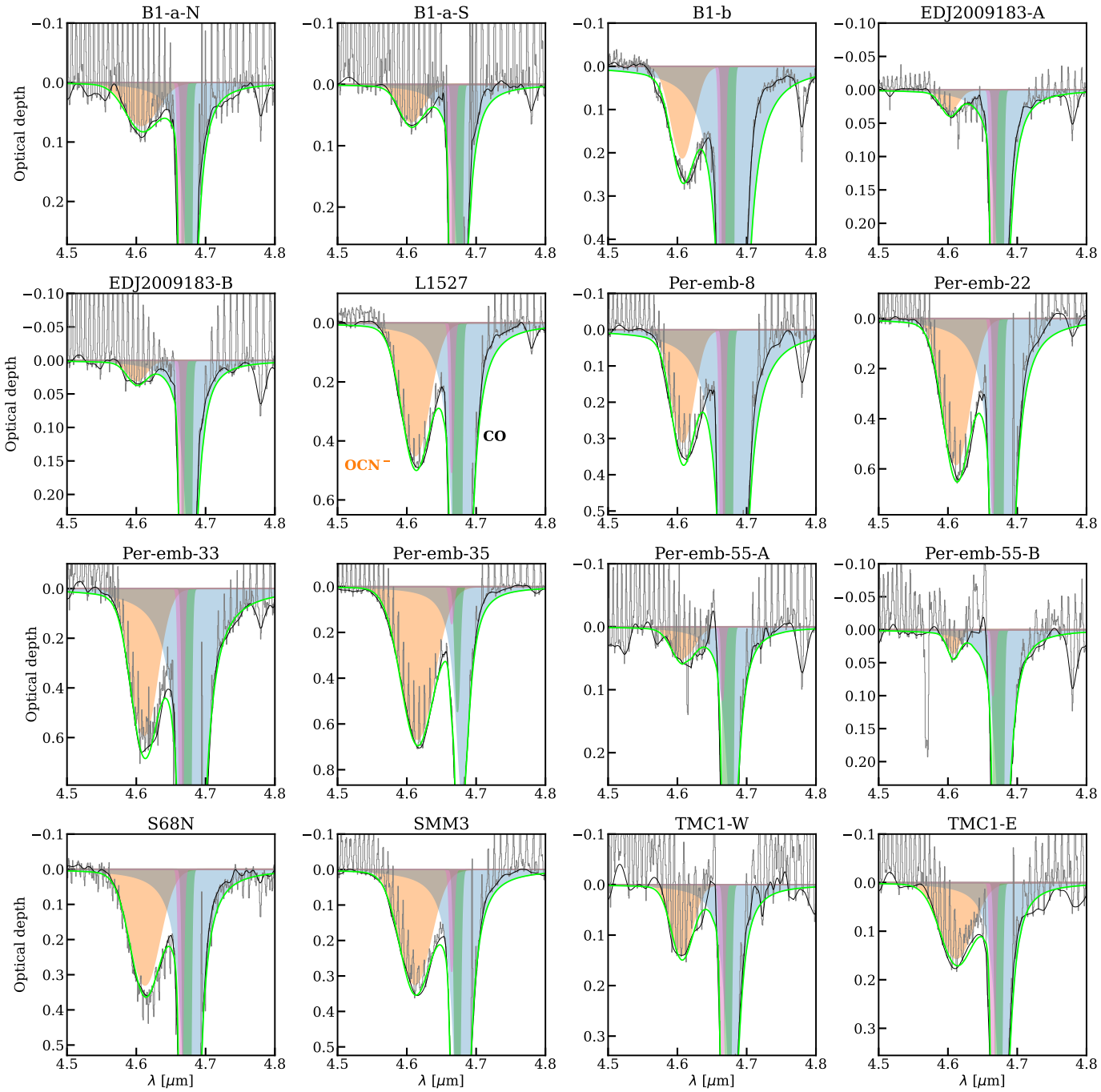


Fig. B.2: Same as the top row of Fig. 2 but for the rest of the objects considered.

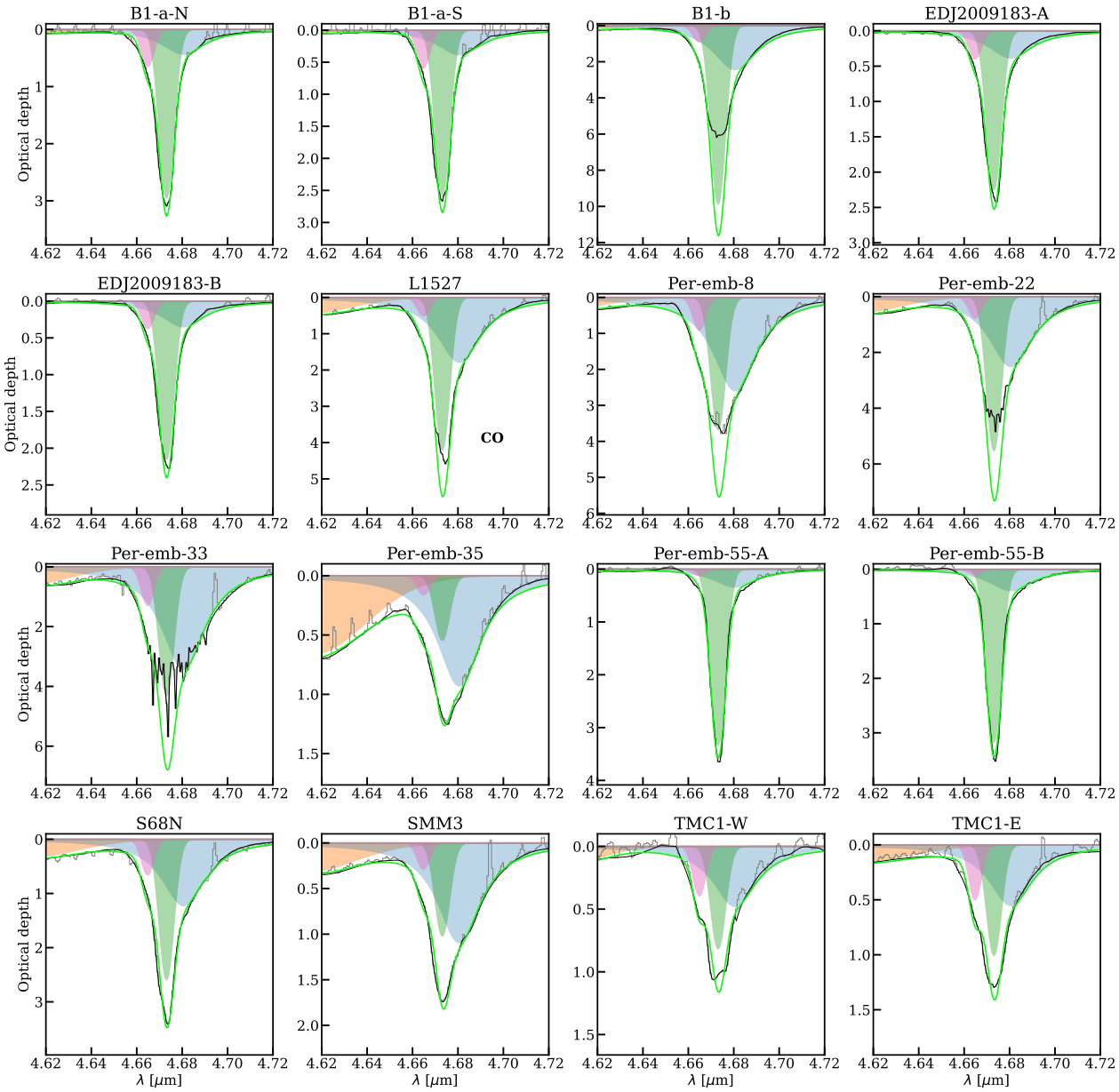


Fig. B.3: Same as bottom row of Fig. 2 but for the rest of the objects considered. The fits that overproduce the bottom of the CO band (i.e., B1-b, L1527, Per-emb-8, Per-emb-22, Per-emb-33), are those where only the wings are fitted because the bottom of the CO feature approaches the noise level in flux scale.

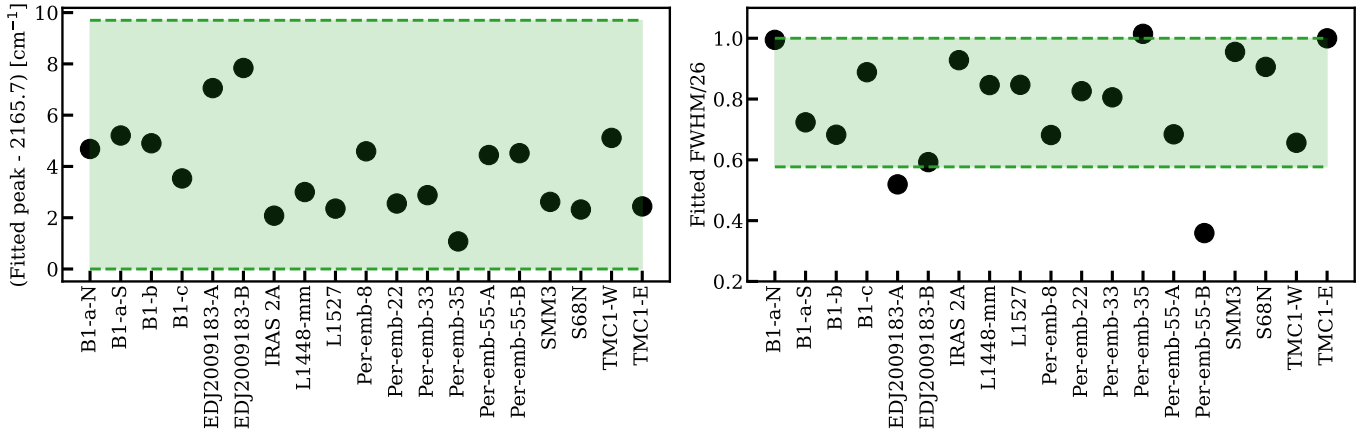


Fig. B.4: Differences between the fitted peak positions (left) and FWHM (right) for $OCN^-$ in this work and the value suggested by van Broekhuizen et al. (2005) for the major component fitted to the 4.6 μm band. The shaded green areas show the difference between the major and minor components used in the two-component fit of the 4.6 μm band in van Broekhuizen et al. (2005). The fitted values mostly fall within this range.

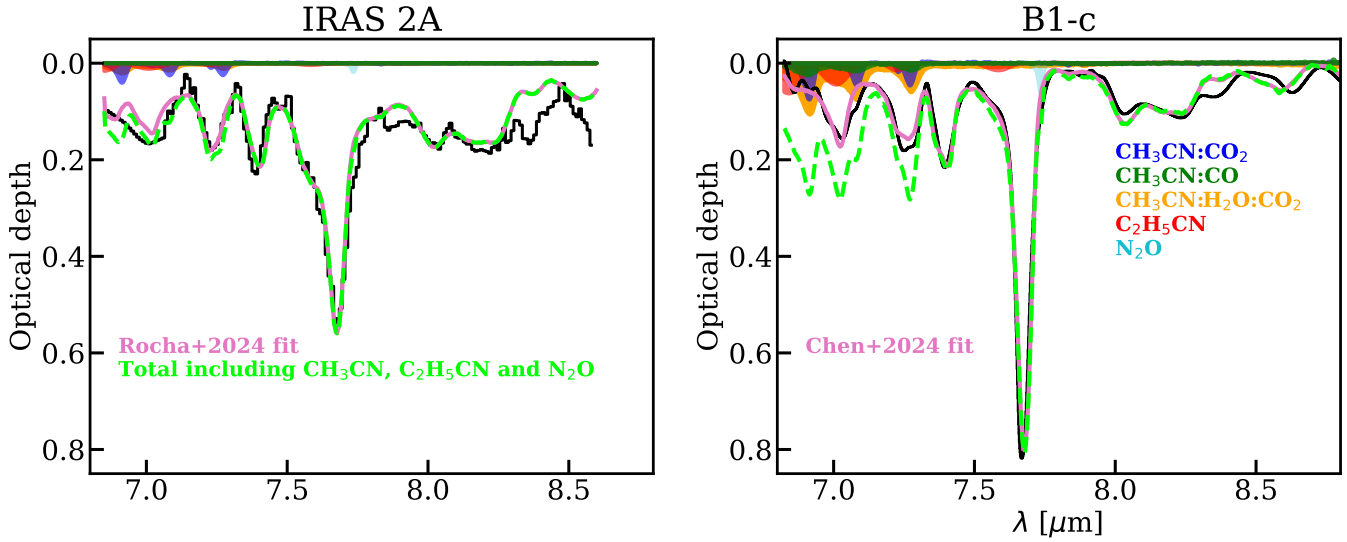


Fig. B.5: Our $CH_3CN$, $C_2H_5CN$, and $N_2O$ fits (same colours as Fig. 3) on top of the total ice fits from Rocha et al. (2024) and Chen et al. (2024) in pink for IRAS 2A (left) and B1-c (right).

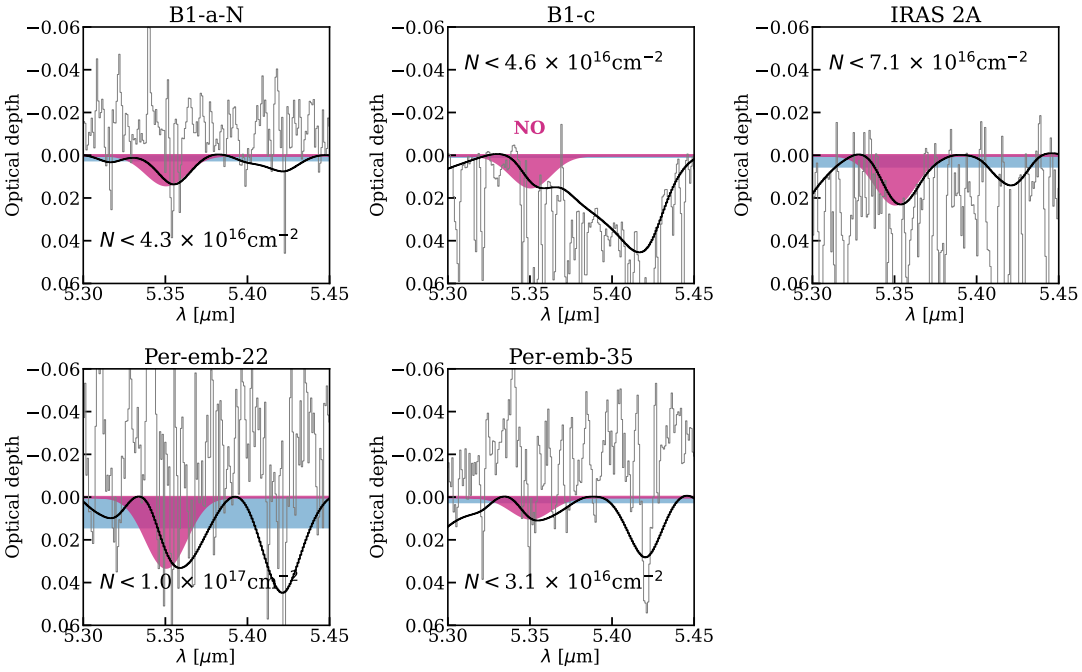


Fig. B.6: Upper limit fits of NO (shaded pink) toward the objects that showed a tentative absorption feature at 5.35 μm. The shaded blue area shows the $3\sigma$ error on the optical depth in the relevant MIRI wavelength range. Gray shows the data and the black line is the fitted spline.

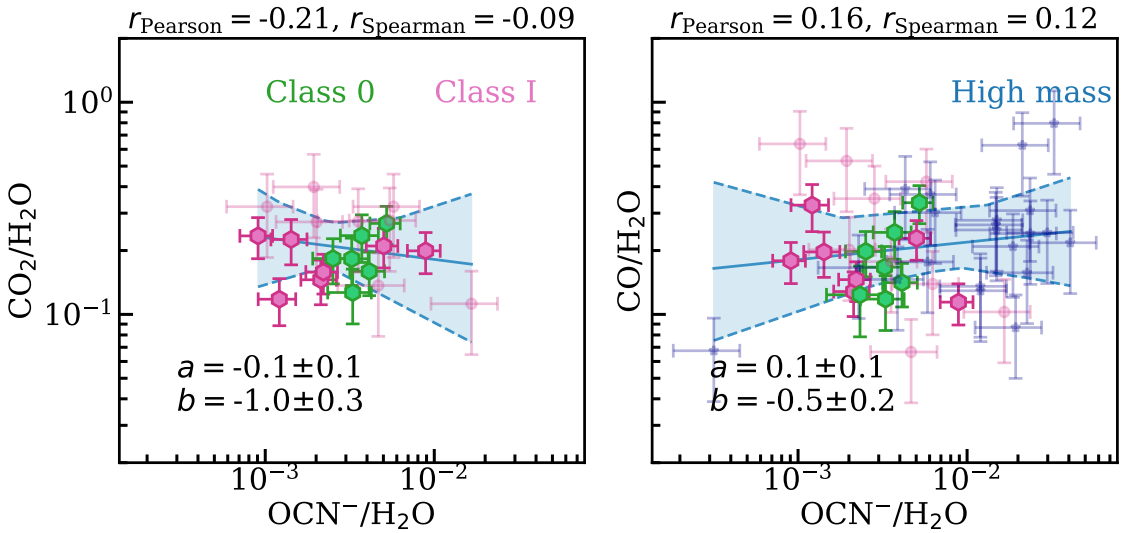


Fig. C.1: Column density ratios of $CO_2/H_2O$ and $CO/H_2O$ versus $OCN^-/H_2O$. The thick hexagons are the JOYS+ JWST results from this work, while the thin circles and stars indicate results from VLT, *Spitzer*, and SpeX for low- and high-mass systems. The $OCN^-$ values are taken from van Broekhuizen et al. (2005) and the CO, $CO_2$, and $H_2O$ are taken from Pontoppidan et al. (2003), Pontoppidan et al. (2008), and Boogert et al. (2008) for low-mass objects. The data for high-mass objects are taken from Boogert et al. (2022). Green shows Class 0 objects, while pink presents Class I objects, and blue presents high-mass objects. The blue solid line shows a fitted straight line to the data and the blue region the uncertainty in the fit. Pearson's $r$ and Spearman's rank coefficient of $\log_{10}$ of the data are printed at the top of each panel. We also fitted a straight line to $\log_{10}$ of the data. The slope ($a$) and intercept ($b$) of each line are printed on the panel.